2019

Unsteady Effects of a Pulsed Blowing System on an Endwall Vortex

Molly Hope Donovan
Wright State University

UNSTEADY EFFECTS OF A PULSED BLOWING SYSTEM ON AN ENDWALL VORTEX

A thesis submitted in partial fulfillment of the requirements for the degree of

Master of Science in Mechanical Engineering

By

MOLLY HOPE DONOVAN

B.S.M.E., Wright State University, 2018

2019

Wright State University

The views expressed in this article are those of the author and do not reflect the official policy or position of the United States Air Force, Department of Defense, or the U.S. Government.

WRIGHT STATE UNIVERSITY

GRADUATE SCHOOL

April 26, 2019

I HEREBY RECOMMEND THAT THE THESIS PREPARED UNDER MY SUPERVISION BY Molly Hope Donovan ENTITLED Unsteady Effects of a Pulsed Blowing System on an Endwall Vortex BE ACCEPTED IN PARTIAL FULFILLMENT OF THE REQUIREMENTS FOR THE DEGREE OF Master of Science in Mechanical Engineering.

_____

Mitch Wolff, Ph.D.
Thesis Director

_____

Joseph C. Slater, Ph.D., PE
Chair, Mechanical and Materials Engineering

Committee on Final Examination:

_____

Mitch Wolff, Ph.D.

_____

Christopher R. Marks, Ph.D.

_____

Rolf Sondergaard, Ph.D., PE

_____

Barry Milligan, Ph.D.
Interim Dean of the Graduate School

ABSTRACT

Donovan, Molly Hope. M.S.M.E., Department of Mechanical and Materials Engineering, Wright State University, 2019. Unsteady Effects of a Pulsed Blowing System on an Endwall Vortex.

The low-pressure turbine is an important component of a gas turbine engine, powering the low-pressure spool which provides the bulk of the thrust in medium- and high-bypass engines. It is also a significant fraction of the engine weight and complexity as it can comprise up to a third of the total engine weight. One way to drastically reduce the weight of the low-pressure turbine is to utilize high lift blades. To advance high-lift technology, the Air Force Research Laboratory (AFRL) designed the L2F blade profile, which was implemented in the linear cascade at AFRL/RQT's low speed wind tunnel facility. The L2F blade has very high lift and an excellent midspan performance, however, it was previously demonstrated to generate significant losses in the endwall region. These losses are primarily driven by the complex time-dependent three-dimensional vortical structures present in the region of the junction of the blade and the endwall, dominated by the Passage Vortex (PV). Aerodynamic flow control is one way to mitigate these losses. Previously, a pulsed endwall blowing system was implemented in the endwall region of the L2F blade which produced a loss reduction. This loss reduction was dependent on the pulsing frequency. In this research, the vortical structures for the baseline flow were characterized with respect to time. The time dependent behavior of the passage vortex motion, location, and strength were found for each pulsing frequency to determine a relationship with total pressure loss reduction. The flow through the passage of the tunnel was characterized with respect to time using high-speed stereoscopic particle image velocimetry. The flow for each test condition was characterized using Q-criterion to determine the strength of the passage vortex and its time dependent behavior. It was found that the passage vortex loses and gains strength in an unsteady manner at time scales between $1.9 < \Delta T+ < 6.7$. The

largest total pressure loss reduction was found to correspond to the pulsing frequency at which the passage vortex was the weakest and moved the closest to the suction surface of the passage.

Table of Contents

List of Figures

List of Tables

Acknowledgments

I would like to thank the turbomachinery branch at AFRL for sponsoring the DAGSI project that this research was completed through. Their facilities made this research possible. I would like to also thank DAGSI and AFRL for funding this research, without it I could not have completed this work.

More specifically I would like to thank Dr. Chris Marks, Dr. Rolf Sondergaard, and Dr. Wolff for their guidance throughout this entire project. They were always available to provide insight and answer questions whenever I had any. I would also like to thank my fellow graduate students who helped me complete this research. Jacob Dickel and Emma Veley provided a great deal of advice and shared their knowledge with me when I began researching at the Low Speed Wind Tunnel facility. I would also like to thank Nathan Fletcher and 2nd Lt. Horatio Babcock. Nathan Fletcher completed the research that set the groundwork for this thesis and was always willing to lend a hand or provide a second opinion when I was stuck on something. Horatio Babcock played a vital role in the data collection that was the key component in this research.

Lastly, I would like to thank my friends and family for their support while I have completed this research. Their patience and understanding during this time-consuming project and stressful time is what allowed me to complete this project and degree.

Nomenclature

A	Area [m^2]
AFRL	Air Force Research Laboratory
BR	Blowing ratio
C_x	Axial Chord [m]
C_μ	Momentum coefficient
D	Diameter [m]
f	Frequency [Hz]
F	General vector quantity
F^+	Non-dimensional frequency $[f\ SSL/U_{avg}]$
H	Span [m]
ILES	Implicit Large Eddy Simulation
k	Number of points inside R
LSWT	Low Speed Wind Tunnel
M	Point in R
MAD	Mean average deviation
MR	Mass ratio
n	Number of points
N	Number of jet holes
P	Point in measurement domain

PV	Passage Vortex
Q	Q-criterion
Q_p	Peak or maximum Q
$\overline{Q}$	Mean Q-criterion
$\overline{Q_p}$	Mean Q-criterion
R	Two dimensional are surrounding P
Re	Reynolds number $[\rho U_{in}/\nu]$
s	Length of a curve [m]
S	Spacing or pitch [m]
SSL	Suction Side Length [m]
t	time [s]
T	Period [s]
T^+	Non-dimensional time $\left[t\ U_{avg}/SSL\right]$
ΔT^+	Change in non-dimensional time
TKE	Turbulent kinetic energy [m^2/s^2]
u	axial velocity [m/s]
$\overrightarrow{U}$	Velocity vector [m/s]
$\overline{U}$	Mean velocity [m/s]
$\bar{u}$	Mean velocity in the x-direction [m/s]
v	pitchwise [m/s]
u’	Velocity fluctuations in the x-direction [m/s]
$\bar{v}$	Mean velocity in the y-direction [m/s]
v’	Velocity fluctuations in the y-direction [m/s]

$\overline{w}$	Mean velocity in the z-direction [m/s]
w’	Velocity fluctuations in the z-direction [m/s]
W	Window size
y’	Pitchwise location [m]
z	Spanwise location [m]
$\hat{z}$	Unit normal vector to measurement plane
Z_w	Zweifel coefficient
Greek	
α	Flow angle [°]
ρ	Fluid density [kg/m^3]
γ	Pressure loss coefficient (16)
Δγ	Change in pressure loss coefficient
Γ	Circulation (16)
Γ_1	Strength of the center of rotation at a point
Θ	Angle between $\vec{U}$ and vector between PM
ω	Vorticity [rotations/s]
Subscripts	
in	Inlet condition
jet	Jet condition
max	Maximum value
MS	Midspan
p	Peak
ps	passage

STD	Standard deviation
t	Total

1. Introduction

1.1 High-lift blade background

The low-pressure turbine (LPT) is a critical component in the design of a gas turbine engine. The performance of the LPT can have a large impact on the performance of the overall gas turbine engine. The LPT can consist of up to one third of the total engine weight making it one of the heaviest components in the entire engine. Since the LPT powers the fan in the gas turbine engine, it is also indirectly responsible for producing up to eighty percent of the total engine thrust [1]. Therefore, the LPT's efficiency can play a significant role in the overall fuel efficiency of the gas turbine engine. Recently, the efficiency of the LPT has become even more important. This is because not only does it power the fan, but it is being used to drive a generator to provide electrical power for the ever-increasing amount of electronics on-board such as communication and diagnostic equipment present on modern aircraft [2].

Engine weight reduction has been an important topic of research since there is a strong relationship between the weight of an engine and amount of fuel the aircraft consumes. One way to impact the overall engine weight would be to reduce the weight of the LPT since it can encompass such a large percentage of the overall engine weight. One effective way to drastically reduce the engine weight is by reducing the number of blades in the LPT. If fewer blades are used, each blade would be required to have a higher aerodynamic loading to achieve the same power output. An example of a high-lift LPT blade that has

been studied extensively is the L2F blade profile. The high-lift L2F blade was designed as a research LPT blade for testing in a linear cascade at AFRL. The L2F is a high-lift front loaded blade profile. It has excellent midspan loading and efficiency, however, it has been shown to generate significant losses in the endwall region. These losses are due to the complex three-dimensional vortical structures present in the endwall region.

There are three distinct losses that occur in the LPT, as well as other turbomachinery components. These losses include profile, endwall, and tip clearance losses. Typically, the endwall secondary flow losses comprise 30-50% of the total losses in a blade row [3]. The losses that occur in the endwall region of turbine blades are due to the complex vortical structures present in that region. These structures can also lead to the loss of lift on a blade, meaning the turbine would produce less net work out [4].

1.2 Time-averaged flow field around turbine blades

A great deal of research has been conducted in an attempt to characterize the flow the surrounding turbine blades. There are many different vortical structures present in the endwall region of turbine blades. One of the most significant ones is the horseshoe vortex. A horseshoe vortex forms at the junction of the leading edge of the blade and the endwall [5]. At this junction the inlet boundary layer meets the leading edge of the blade, causing it to roll-up and form the horseshoe vortex [3, 5-7]. The horseshoe vortex entrains most of the fluid present in the inlet boundary layer. This phenomenon is well understood, because it is rooted in the same phenomena that occurs at the junction of a cylinder and a flat plat [8]. A horseshoe vortex has two sides and in turbine applications they are called the pressure and suction side legs. Each leg rotates in a opposite direction [3].

There is a pressure gradient that spans across the passage from the pressure side to the suction side of the adjacent blade. Increasing loading on LPT blades has been found to lead to a larger pressure gradient [9]. This pressure gradient is caused by the curvature of each passage [10]. This pressure gradient drives the pressure side leg of the horseshoe vortex to travel across the passage [3-5, 7, 10, 11]. The pressure side leg of the horseshoe vortex entrains fluid as it is fed across the passage, leading it to grow into the passage vortex (PV) [3-6]. The pressure side leg of the horseshoe vortex has been given the name the PV because it spans across the passage from the pressure side to the suction side [10]. The PV combines with the crossflow present in the endwall region of the passages, and increases in size [5,6]. This occurs until it impinges on the suction surface of the adjacent airfoil and moves up the suction surface [5]. At this point, the PV also combines with the suction side corner separation vortex, creating a very complex flow structure [7]. The specific location, strength, and shape of the PV are dependent on the geometry of a particular blade [8].

The same two flow mechanisms (secondary flow and the radial pressure gradient), which strengthen the pressure side vortex weaken the suction side of the horseshoe vortex [10]. The suction side travels into the adjacent passage with a rotation opposite of the PV. The suction side is also much smaller than the pressure side [4]. It has been found to have a weaker swirl strength and to be greatly influenced by the strength of the PV [8,12]. The suction side leg continues along the suction side of the blade until it interacts with the PV and the wall jet that the PV creates [3, 12]. The suction side of the horseshoe vortex also greatly influenced by the strength of the PV [8].

The endwall region of turbine blades is a location of significant losses [11]. The PV contributes significantly to the losses in this region. Near the suction side of the adjacent blade, the PV interacts with the flow in that region leading to losses [6,11]. Significant losses occur in the region where the PV and endwall flows interact with the suction surface boundary layer [6, 13]. Previous low speed linear cascade testing revealed that a total pressure loss reduction is obtained when the PV is weakened. Also, it was found that a stronger suction side corner separation vortex results in a total pressure loss reduction [13].

AFRL developed a high-lift front loaded research blade, called the L2F. The front-loading of the L2F blade further aggravates the losses in the endwall region [2]. But, the advantage of a front-loaded blade is that front loading typically mitigates the profile losses in the midspan region of the blade at low Reynolds numbers. Understanding the losses in the endwall region has been critical to identifying mechanisms driving the overall losses. Insight into what drives these loss mechanisms allows for more effective designs which mitigate the losses and control the structures driving them [10]. The junction of the endwall region and the blade is an area characterized by high loss production because this is where the PV meets the 3D separation, caused by the separated boundary layer [12].

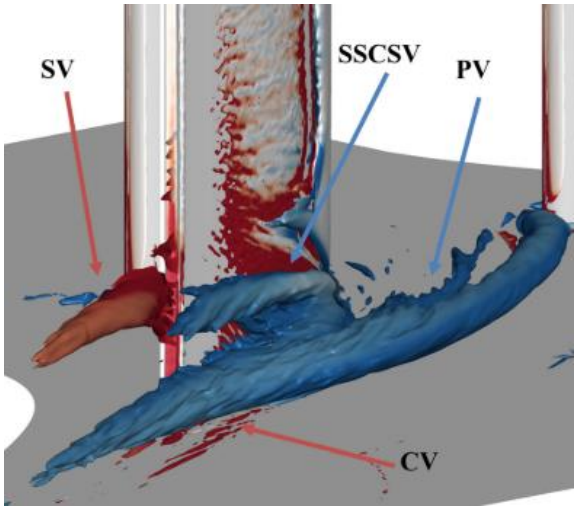

Figure 1: Flow structures around the L2F passage [11].

The endwall boundary layer affects the mean flow field in the passage surrounding the L2F blade [14]. A series of detailed experimental endwall flow studies using the L2F blade profile have been conducted at AFRL. These studies used a low speed linear cascade with seven L2F blades to better understand the relationship between endwall flow structures and loss generation. A splitter plate was implemented in the linear cascade, to provide control of the incoming boundary layer. The splitter plate created an endwall ensuring that the boundary layer was both clean and had a known thickness of 9.3% $C_{x.}$ To track the PV through the entire passage, the PV lift off line was found using oil flow visualization.

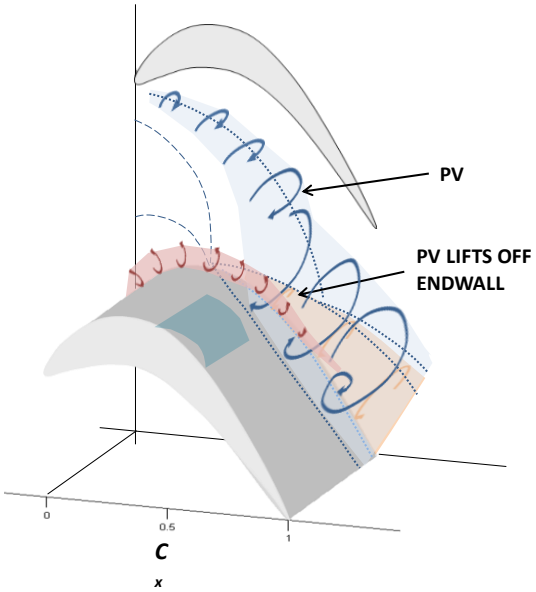

Figure 2: PV Lift off line in L2F passages [12].

The PV lift off line moves downstream as the Reynolds number increases. The PV lift off line is essentially the mean location of the core of the PV and it verified that the PV travels from the pressure side to the suction side of the blade.

1.3 Unsteady LPT research

It has previously been noted that the flow behavior in the passages of the L2F blades is inherently unsteady. This is especially true for the PV. The unsteady behavior of the PV propagates through the passage as the overall flow travels through the passage. Implicit Large Eddy Simulations (ILES) have been performed in an attempt to model and characterize the flow through the passage. The goal of these studies was to characterize the

complex structures present in the endwall region which dominate the production of losses. It was found that there are low frequency oscillations present in the passage that stem from the junction flow region at the leading edge. This region affects the PV since it originates at that point and propagates downstream under the influence of the bulk flow and passage pressure gradients. Proper orthogonal decomposition was performed on the results from the ILES simulations. This demonstrated that the passage vortex coherence is actually due to the bimodal behavior of the horseshoe vortex immediately in front of the leading edge [10]. Instantaneous plots of the velocity from earlier particle image velocimetry (PIV) experiments demonstrated that the PV moves in an unsteady manner in both the pitchwise and spanwise directions [12]. This validated the results from the ILES simulations.

Understanding the time dependent flow mechanisms in the endwall region is critical to improved LPT performance. Previously acquired unsteady data has allowed for better computational models and tools to be developed as well as designs to mitigate the losses by controlling the structures that are leading to the losses [15]. Non-intrusive surface mounted hot-film sensors were developed at the LSWT facility to detect unsteady velocity fluctuations [16]. These sensors were utilized to measure the unsteady fluctuations in the flow near the endwall and the junction of the blade [15]. Traditional hot-films and hot-wires have blockage effects on the flow. Since the non-intrusive hot-films are mounted on surface, they do not have the same issues as traditional hot-films or hot-wires [16]. Therefore, the data acquired is more representative of the actual flow using the non-intrusive sensors.

In the research of Veley et al, the surface mounted hot-film sensor locations were selected based on the location of the passage vortex lift off line [15]. This research was to

confirm the results from ILES simulations. The ILES simulations predicted that the PV moves in both the pitchwise and streamwise directions and loses its coherency intermittently, but the exact times scales at which these events occurred were not known experimentally.

The endwall sensors found fluctuations on the endwall in the region of the PV that were the strongest over the frequency band centered around 22 Hz (Figure 3). The frequency of the fluctuations roughly matched the ILES results. Based on the agreement between the experimental and computational results, the fluctuations correspond to the intermittent bursting and reforming events of the PV.

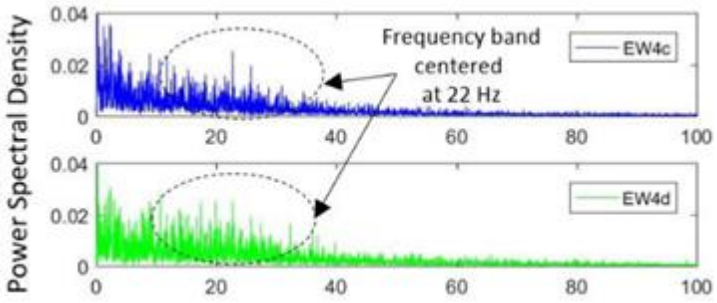

Figure 3: PSD of hot-film sensors [15]

1.4 Flow control background

Mitigating high loss regions surrounding high lift blades is key to practical application in actual LPTs. One popular method which has been studied by various researcher's is flow control. The term "flow control" is used to describe methods of changing (i.e. controlling) the flow to mitigate these losses. Flow control methods are typically broken down into two major subcategories: passive and active. Passive flow control includes approaches that are permanently fixed onto a blade or LPT, i.e. blade or endwall contouring. These methods can be attractive because they are relatively simple and easy to implement in an LPT. They are usually optimized for a specific (design) flow condition [9]. Active methods usually are considered more advantages even though they introduce additional complexity. These

methods have the advantage that they can be changed (i.e. controlled) for in flight conditions at the cost of additional complexity.

Many different methods of flow control have been tested with respect to low pressure turbines [7]. Bons et. al. found that there were a few main categories or methods to control the flow through the passage using active flow control and these include: streamwise vorticity generation, enhancing the natural instabilities in the flow, using suction to remove the boundary-layer, and streamwise momentum injection. In addition, PV removal through suction and/or redirection has been tested. For PV removal, endwall holes were placed near the PV path. For PV redirection the suction holes in the endwall were placed closer to the pressure side of the blade. It was shown that blowing could move the loss generating structures to areas which minimized the overall LPT losses.

Bloxham et al. implemented vortex generator jets at the midspan of the blade to reduce profile losses [17]. Profile losses can account for a significant portion of the total pressure loss, but usually less then endwall losses. It was found that the vortex generator jets induced boundary layer transition and created streamwise vortical structures. Both effects pulled fluid from the freestream into the boundary layer which reduced flow separation and profile losses.

Synthetic vortex generator jets were implemented at the United States Naval Academy [9]. In this research, the jets were directly placed on the suction side of a turbine blade. The jets were drilled directly into the suction surface of the blade. Each jet had a diameter of 0.8 mm and were spaced 8.5 mm apart. Each hole was drilled at a 90° angle to the main flow through the passage and at 30° in pitch to the suction surface. It was shown that a high amplitude jet velocity was required to have a large influence on the boundary layer. At low

Reynolds numbers, the synthetic vortex generator jets were found to be effective for controlling the separation of boundary layers. They prevented separation by transporting the high momentum fluid into the boundary layer and increasing turbulence. It was also shown that vortex generator jets were successful at forcing the separated boundary layer to reattach.

Aunapu et al. installed jets into the endwall region and tested various configurations [5]. The jets had a 6 mm diameter [5]. The jets led to additional secondary losses because they introduced additional turbulence into the passage. The pressure loss was not actually generated by the PV, but instead near the endwall corner of the suction surface. The loss was due to the fluid in this region becoming entrapped with the PV. The jets did change the path of the pressure side leg of the horseshoe vortex; however, they did not weaken the vortex strength. Instead the jets blocked the vortex and prevented it from traveling across the entire passage.

Acoustic excitations were used to influence the boundary layer by Bernardini et al. [18]. A speaker was driven by a signal generator and connected to an amplifer. This was used to produce excitations in a sine wave pattern at a specific discrete frequency. They discovered that the most effective frequencies were near the natural instability of the shear layer. Additionally, excitations at the unstable frequencies intensified the shedding of the vortical structures into the shear layer by transporting fluid with high momentum towards the wall. Also, the inlet turbulence greatly impacted the effectiveness of the system. Finally, the effectiveness of the acoustic excitations was reduced as the Reynolds number increased. All these active control methods demonstrated the feasibility for loss reduction

in LPT systems. These methods were not applied to a high lift front loaded LPT blade like the L2F blade which creates a unique set of vortical structures.

1.5 Flow control at LSWT facility

Many types of flow control methods have been studied in the linear cascade at the AFRL/RQT LSWT facility. Methods of passive endwall flow control were tested on the L2F blades. These included profile contouring and endwall contouring. The profile contouring of the L2F-EF was found to reduce the total pressure loss. This reduction in losses was due to the weaker PV. It was believed that weaker passage vortex could be attributed to a weaker cross-passage pressure gradient. This gradient is responsible for driving the PV across the passage. The passage flow within the L2F-EF contour was also modeled using ILES. These results confirmed the hypothesis that the contour weakened the PV. A second profile contour design, the L2F-EF2, was implemented in the linear cascade. This contour forced the PV upstream and led it to impinge on the suction surface sooner. The impingement caused the vortical structures present near the suction surface to reduce in both strength and size [12]. Profile contouring was found to be an effective method of passive flow control, however, in an attempt to mitigate the losses even further, endwall contouring was also tested.

Endwall contouring was implemented at the LSWT facility at AFRL [19, 20]. An example of an endwall contour tested is shown in Figure 4. Experimental testing in a linear cascade showed that the endwall contour produced a total pressure loss reduction of 7.8%. This compared well to the numerical results which predicated a reduction of 8.2%. The losses in the endwall region were reduced even more significantly with a 19.9% improvement. This was only slightly lower than the prediction of 22.9% found using the

Reynolds Averaged Navier-Stokes model [20]. A genetic algorithm was used to optimize the endwall contour. The algorithm controlled forty different variables and used 2500 total design cases across twenty-five generations. A second, optimized contour was found using this method. This contour led to a loss reduction of 8.6%. The experimental result was slightly below the numerical prediction of 10.6% [19].

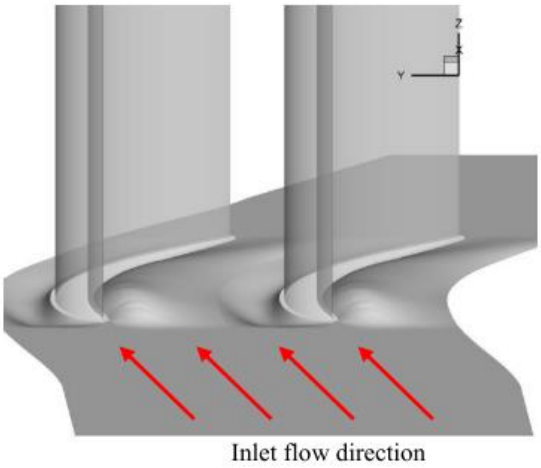

Figure 4: An example of an endwall contour tested in the LSWT [20].

An endwall blowing system was also implemented in the endwall region of the L2F blade. Both steady and pulsed endwall jets were tested. It was found the steady jets produced the maximum reduction in total pressure loss, however, these jets used high mass ratios. Meaning that the steady jets utilized a large volume of air. Pulsed jets were found to produce a total pressure loss reduction higher than the steady jets with similar mass ratios. The total pressure loss reduction for pulsed cases were also found to vary for different pulsing frequencies. This was true even when the momentum coefficient, blowing ratios, and duty cycles were all held constant [21]. This implies that the effectiveness of the system also has a component of frequency dependence.

1.5.1 Total pressure loss

Total pressure loss can be used to represent the efficiency of the flow through the linear cascade. The total pressure loss reduction from the baseline flow was calculated for each of the pulsing frequencies. The method for calculating the total pressure loss coefficient

can be found in Equation 1. The inlet total pressure and inlet velocity was found by measuring the dynamic pressure with a Pitot-static probe. The probe was placed $2C_x$ upstream of the leading edge of the linear cascade. A pressure rake consisting of five inline total pressure probes was used to find the exit total pressure. This rake was traversed in the region $1.5C_x$ downstream of the leading edge of the blades, and recorded measurements across one pitch and 40% of the span [21]. The total pressure loss measurements that were taken measured 38% of the entire pressure loss in the passage [21].

$$\gamma_t = \frac{p_{t,in} - p_{t,out}}{\frac{1}{2}\rho U_{in}^2} \quad \textbf{(1)}$$

Figure 5 shows the total pressure loss reduction which was defined as the reduction in the total pressure loss from the baseline case for various pulsing frequencies The duty cycle and velocity of the endwall jets were held constant. The only condition that was varied was the pulsing frequency. From this plot, the total pressure loss reduction is dependent upon the pulsing frequency. Based on Figure 5, the total pressure loss reduction increases as the pulsing frequency increases. The maximum loss reduction is at a pulsing frequency of $F^+ = 1.2$. The detailed effects on the flow structures from the pulsed endwall jets were not investigated. Therefore, the physics driving the frequency dependence remained unknown.

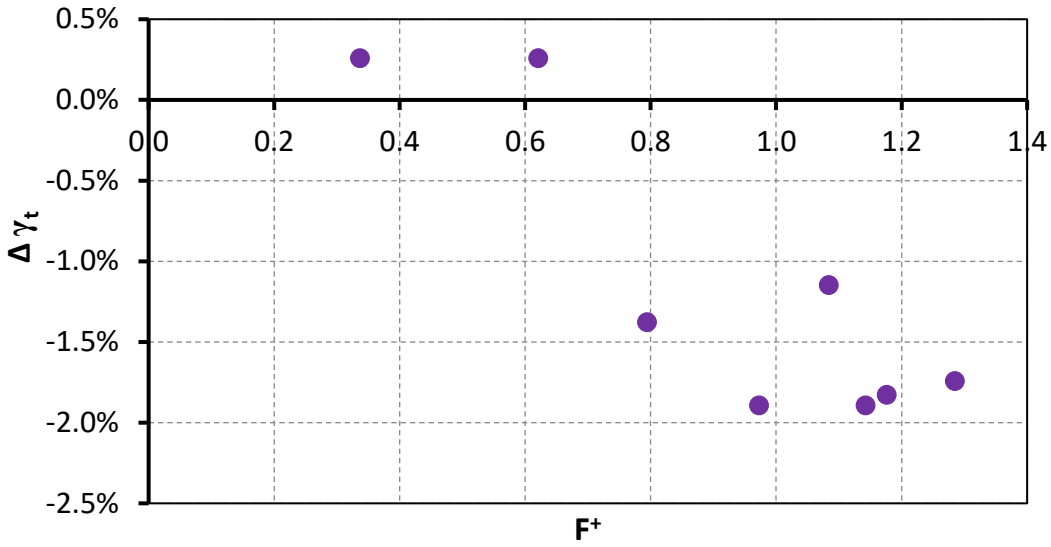

Figure 5: Total pressure loss reduction for different pulsing frequencies.

1.5.2 Exit angle

An LPT row has a designed exit angle. Any deviation from the designed exit angle can impact the efficiency or performance of the entire gas turbine engine. The complex flow structures present in the endwall region of the L2F blade were found to cause the actual exit angle of the flow to deviate from the ideal. Since the blowing system effected the endwall region, the system may also affect the exit angle. Therefore, the exit angle was investigated. This provided an additional measure of effectiveness.

The mass averaged flow exit angle at the blades midspan was calculated using Equation 2.

$$\alpha_{MS} = \tan^{-1}\left(\frac{v_{MS}}{u_{MS}}\right) \quad (2)$$

Once the mass averaged exit angle at the midspan was calculated the mass averaged deviation (Equation 3) from the midspan angle at points along the span were calculated. This was done for the baseline flow condition as well as for each jet pulsing frequency.

This calculation only accounted for the magnitude of the deviation. It does not differentiate between over and under turning.

$$\Delta\alpha_i = \alpha - \alpha_{MS} \quad \textbf{(3)}$$

The standard deviation of the mass averaged exit angle from the endwall to 40% of the span was calculated by using Equation 4.

$$\alpha_{STD} = \sqrt{\frac{1}{n-1}\sum_{i=1}^{N}\left|\Delta\alpha_i'\right|^2} \quad \textbf{(4)}$$

Figure 6 shows the results for the standard deviation of the improvement of the mass averaged exit angle across the span for various pulsing frequencies. This is the percent change in the overall exit angle deviation. If the baseline deviation from design was 5° and the standard deviation at a pulsing frequency is -10° then the deviation from the design exit angle would be 4.5°. The trend of the exit angle improvement resembled the total pressure loss reduction, Figure 5. The pulsed endwall jets improved the exit angle out of the cascade. The maximum improvement occurred at an endwall jet pulsing frequency of $F^+ = 1.2$. This agreed with the frequency at which the largest pressure loss reduction was measured.

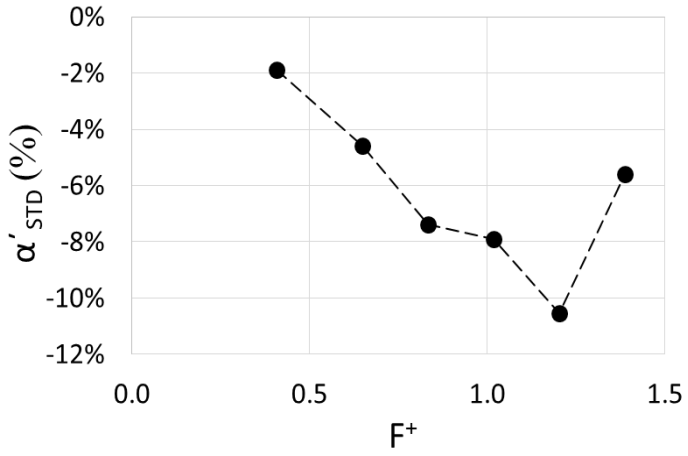

Figure 6: Percent change in overall exit angle deviation

2. Objectives

The overall objective of this research is to determine how the pulsed endwall jets affected the flow through the passage. Specifically, the goal is to determine why the various pulsing frequencies lead to the different reductions in losses and improvements in exit angles. The first step is to fully characterize the baseline flow at a Reynolds number of 100k, corresponding to the Reynolds number that the endwall jet system was previously tested. This is accomplished so that the effects of the pulsed endwall jets can be quantified. Without a complete understanding of the baseline flow the effect of the pulsed jets would not be quantifiable.

In addition, the effect of the jets, on the time dependent behavior of the PV in the flow field needs to be determined. The intended goal of the endwall jet system was to amplify the natural instabilities of the PV to reduce the total pressure loss. The goal in this study was to analyze the flow at each pulsing frequency to determine whether this is the mechanism that led to the loss reduction. Previously, this has not been fully investigated experimentally.

The final goal of this thesis is to characterize the PV behavior at a Reynolds number of 50k. The difference between the flow structures at a Reynolds number of 50k and 100k will be investigated.

3. Experimental Set-up

3.1 LWST facility/tunnel overview

All testing was completed in the linear cascade installed in the ARL/RQT Low Speed Wind Tunnel (LSWT) facility, shown in Figure 7. The linear cascade consists of seven straight high-lift front loaded L2F blade. A splitter plate was placed both upstream and downstream of the blades to produce a clean boundary layer with a thickness of 9.3%C_x.

Figure 7: LSWT Facility at AFRL.

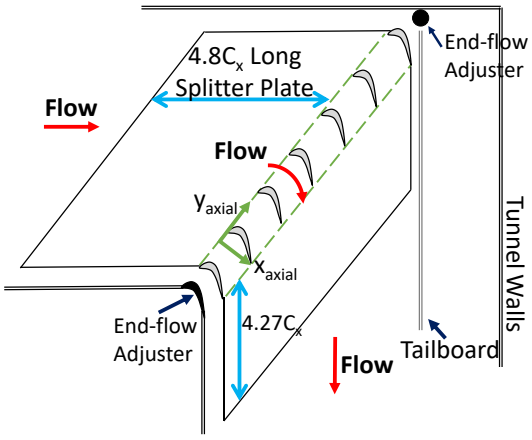

Figure 8: Configuration of the linear cascade.

The overall configuration of the test section of the linear cascade is shown in Figure 8. The speed of the wind tunnel was set referencing a Pitot-static pressure probe that was placed $2C_x$ upstream of the leading edge of the blades, plumbed to a 0-0.4 in-H_2O Druck transducer to measure the inlet dynamic pressure of the tunnel. The Reynolds number was calculated with respect to the inlet tunnel velocity and the blade axial chord. Experimental measurements

for which the results will be presented in the following chapters were taken at Reynolds numbers of 50k and 100k. All measurements for the pulsing cases were conducted at a Reynolds number of 100k. The general parameters for the linear cascade and tunnel condition are provided in Table 1.

Table 1: Dimensions of the linear cascade and tunnel conditions.

Axial chord, Cx	**15.24 cm**
Pitch/axial chord, S/Cx	1.221
Span/axial chord, H/Cx	4.17
Boundary Layer Thickness	9.3%C_x
Inlet flow angle (from axial), α_{in}	35°
Predicted mean profile exit angle, α_{ex}	-58.12°
FSTI	3.0%
Zweifel Coefficient, Zw	1.59
Reynold's Number	1.0 x 10^5/5.0 x 10^4

3.1 Blowing jet configuration

Arrays of seven endwall jets were placed in a circular array near the leading edge of the three center blades in the endwall region along the PV lift-off line. The endwall jets were placed in this location so that they would be able to directly influence the PV. Each jet hole was 1.6 mm in diameter and was drilled into a disc that was inserted into the splitter plate.

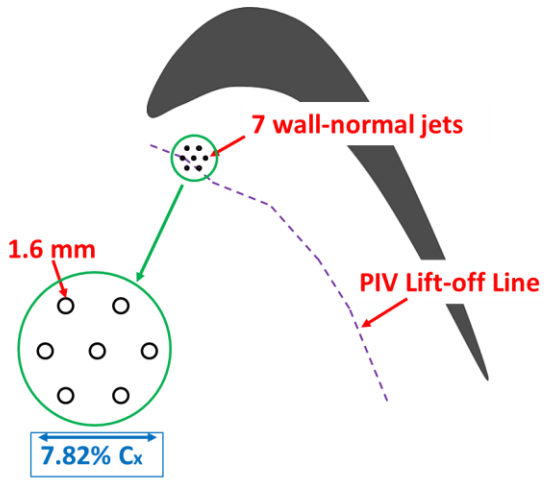

Figure 9: Schematic of the pulsed jet configuration.

The surface of each jet exit was flush with the splitter plate and each hole was normal to the endwall. The blowing angle and placement of the jets were not optimized. The total

diameter of the jet array was 12 mm or 7.8%C_x with the goal of creating a small jet array to apply jet pulsing to a localized area of the flow because of uncertainty in the exact location of the PV. A diagram of the overall configuration of the jets is shown in Figure 9. The locations of each of the jet holes in the passage is given in Table 2.

The jet arrays were placed in the three center passages of the linear cascade. A solenoid valve was used to actuate the endwall jet pulsing in each of the passages. All three of the solenoid valves were controlled using an IOTA One solenoid valve driver. Pneumatic tubing was plumbed directly from the solenoid valve to the jet holes via a tubing manifold. A pressure tank acted as the feed plenum for the system to provide uniform feed pressure. Two regulators were placed upstream of the pressure tank to minimize the pressure fluctuation in the tank that might stem from the cycling of the facility air compressor. A flow meter was also placed upstream of the tank to monitor the amount of air utilized by the pulsed jets. The momentum coefficient of the jets was calculated and used to determine the cost of the overall system. The pulsing frequency, F^+, was non-dimensionalized by the suction surface length and the mean velocity through the passage, which is given in Equation 5. This was done so that the pulsing frequency could easily be compared to the time it would take for the flow to convect through the passage, or the convective time.

Table 2: Location of Endwall Jets.

x/C_x	y/C_x
0.063	0.479
0.083	0.448
0.083	0.510
0.094	0.479
0.120	0.448
0.120	0.510
0.133	0.479

$$F^+ = \frac{f * SSL}{\overline{U_{pass}}} \quad \textbf{(5)}$$

3.2 Jet characterization

The endwall jet blowing system was characterized outside of the linear cascade wind tunnel by using a miniature TSI hot-wire anemometer placed over the centerline of the center jet and controlled by an IFA300. The hot-wire was calibrated up to the maximum velocity expected to be exiting the jet. The mean peak velocity was used to determine the blowing ratio. While the jet array the center whole was used to characterize the velocity, measurements were also taken on the other holes and the variation between each of the holes tested was found to be relatively small, less then 10%. The ensemble averaged velocity was calculated to determine the on and off characteristics of the pulsed endwall jets, also referred to as the duty cycle of the jets. It was found that an input duty cycle of 45% into the solenoid valve driver led to a measured duty cycle of 50±5%. The duty cycle is defined as the time the jets are firing vs the time the jets are ejecting no air. An example of the velocity trace of the center jet for the pulsing frequency of $F^+ = 1.2$ is shown in Figure 10. It is clear the actuation of the jets is clean and strongly resembles a square wave driving the jets. Also, the endwall jets are on for roughly 50% of the pulsing period, which was the goal.

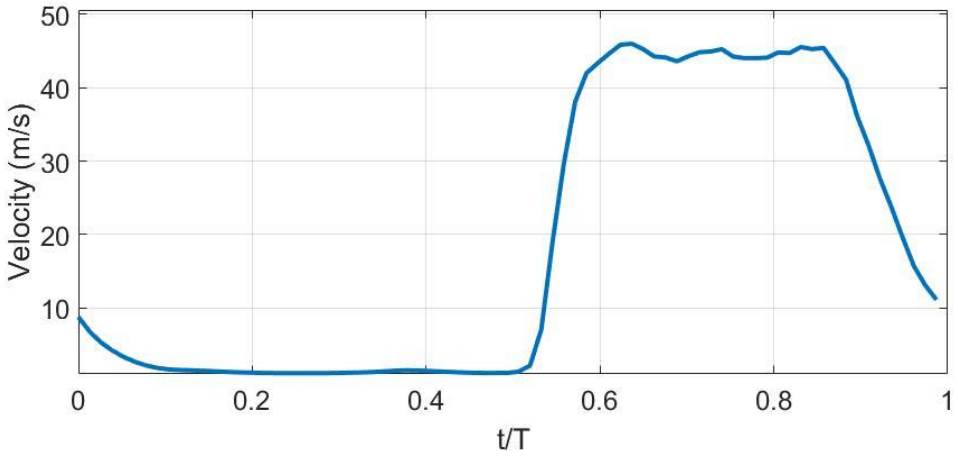

Figure 10: Velocity profile of the center jet for F+ = 1.2 pulsing case.

The jets were characterized for variations in the blowing ratio (BR), momentum coefficient, and the non-dimensional frequency. The BR represents velocity of the jets. It is defined as the ratio of the average maximum velocity of the endwall jets to the average inlet velocity of the tunnel, Equation 6. For all the pulsed cases, the blowing ratio was 4.3±1.

$$BR = \frac{\overline{U}_{jet,max}}{\overline{U}_{in}} \tag{6}$$

In an operation engine, the air for pulsed endwall blowing system is expensive since it would be taken from the compressor, bypassing the combustor, and is not used to produce thrust. The mass ratio (MR) represents the amount of air injected into the passage compared to the mass of the air passing through half the span of the blade. The MR is found using Equation **7**, and was 0.058±5%. Therefore, a relatively small amount of air would need to be redirected to implement this system.

$$MR = \frac{1}{2}\overline{\left(\frac{U_{jet}}{U_{in}}\right)^2}\,\frac{\pi N D_{jet}^2}{HS\cos(\alpha_{in})}x100\% \tag{7}$$

The final parameters that is used to characterize the endwall jets in this study is the momentum coefficient, Equation 8. The momentum coefficient represents the ratio of the momentum influx into the passage from the jets to the general momentum influx in half of the passage. The momentum coefficient was 0.21±3%.

$$C_\mu = \frac{\rho_{jet}\overline{U_{jet}^2}\left(N \cdot A_{jet}\right)}{\rho_{in}\overline{U_{in}^2}\frac{1}{2}\,(H \cdot S)\cos(\alpha_{in})} \times 100\% = \frac{1}{2}\overline{\left(\frac{U_{jet}}{U_{in}}\right)^2}\,\frac{\pi N D_{jet}^2}{(H \cdot S)\cos(\alpha_{in})} \times 100\% \quad \textbf{(8)}$$

The exact non-dimensional frequency, duty cycle, blowing ratio, momentum coefficient, and mass ratio for each pulsing condition is shown in Table 3.

Table 3: Parameters of the endwall jets for various pulsing frequencies.

F+	f (Hz)	DC (%)	BR	C_μ (%)	MR (%)
0.16	15	47	4.3	0.19	0.053
0.27	25	49	4.3	0.22	0.057
0.38	35	50	4.3	0.22	0.059
0.49	45	53	4.3	0.23	0.060
0.60	55	54	4.4	0.24	0.061
0.71	65	55	4.3	0.23	0.060
0.82	75	55	4.3	0.22	0.059

3.3 Hot-films

Eight surface mounted hot-film sensors were placed directly on the endwall $0.92C_x$ downstream of the center jet in the endwall blowing system. Two additional hot-film sensors were placed next to the leading edge of the blade. The placement of the sensors is shown in Figure 12. The surface mounted hot-

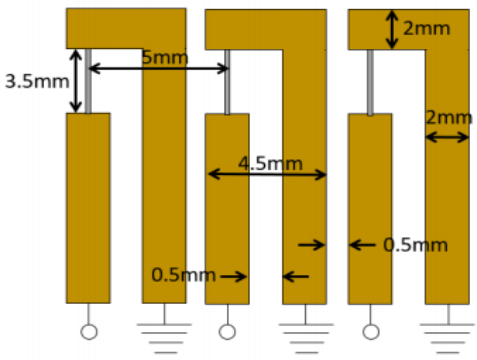

Figure 11: Hot-film sensor array dimensions.

film sensors consist of a platinum sensor deposited on Kapton tape and controlled by an IFA300 constant temperature anemometer. The sensors were previously developed and manufactured in house. An example of their dimensions are shown in Figure 11 [22].

The lead wires of the hot-film sensors were secured so that they would not interrupt or disturb the flow field. Sensors were placed across the PV lift off line and were calibrated so they would not overheat. Sampling was at 15kHz with a high pass filter of 0.1 Hz and a low pass filter of 2kHz used. The power spectral densities of the voltage measured for each sensor was calculated using a Fast Fourier Transform.

Table 4: Locations of the surface mounted hot-films.

Sensor	x/C_x	y/C_x
LEa	-0.06	0.60
LEb	-0.08	0.63
EWa	0.53	-0.31
EWb	0.56	-0.29
EWc	0.58	-0.27
EWd	0.62	-0.25
EWe	0.64	-0.23
EWf	0.67	-0.22
EWg	0.70	-0.20
EWh	0.73	-0.18

3.4 SPIV and Flow Visualization Setup

Stereoscopic particle image velocimetry (SPIV) data was captured in a plane slightly upstream of the location of the hot-film sensors and aligned with them. The plane was also perpendicular to both the exit flow direction and the mean axis of rotation of the PV. A diagram of the placement of the SPIV plane is shown in Figure 12. Two Phantom VEO 640L cameras fitted with Scheimpflug adapters were used to capture the data. The cameras had a full

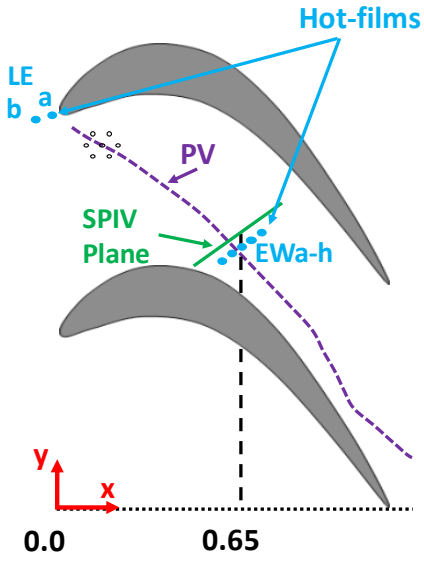

Figure 12: Diagram of SPIV and hot-film locations in passage.

resolution of 2560x1600 pixels but the area sampled on the image sensor was restricted to 1401x1002 pixels to allow the cameras to capture at a higher repetition rate. The first camera was placed at an angle (7.52, 65.2, 9.32)° relative the calibration plate. The second camera was placed an angle (1.20, 209, -0.551)° relative to the calibration plate. The camera focal lengths were 223 mm and 114 mm, respectively. The overall magnification factor was 14.5 px/mm. A high-speed Photonics Laser model DM30-527DH was fitted with sheet forming optics to produce the laser sheet. The laser was operated at 5kHz for the Flow Visualization and 2.5kHz for the SPIV. The data acquisition system was controlled by a programmable timing unit (PTU) made by LaVision. For the SPIV a Martin JEM ZR25 was used upstream of the wind tunnel to seed the flow with Pro Smoke Super Fluid as the seeding substance. The set-up of the SPIV system is shown in Figure 13.

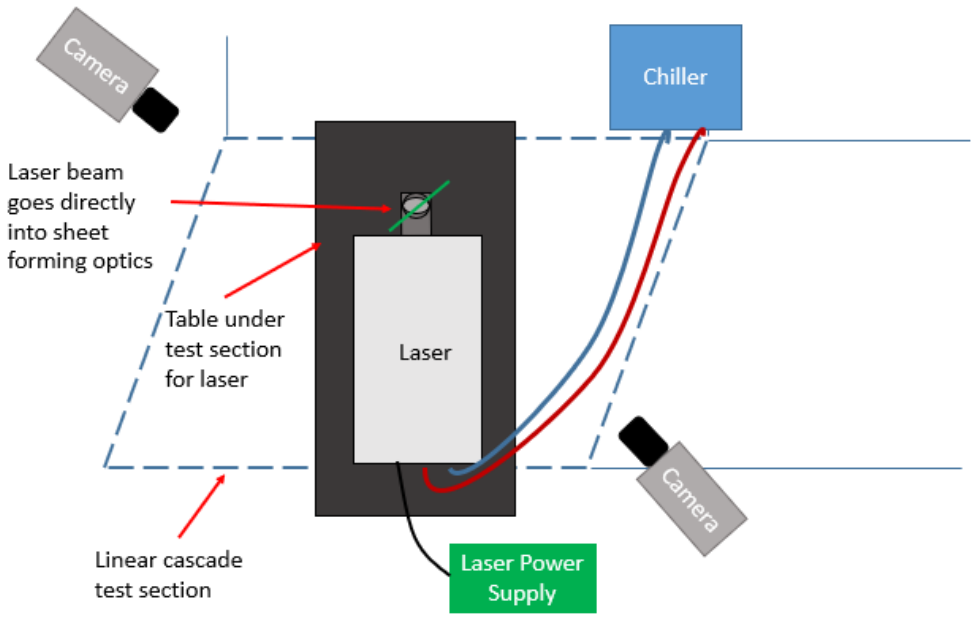

Figure 13: Schematic of the SPIV set-up.

The raw images were processed using DaVis 8.4. A geometric mask and minimum light intensity filter was applied to each image. A GPU was used to process the images with a

square investigation window of 64x64 pixels on the first pass. Three additional passes were conducted with circular 32x32 pixel window sizes and a 50% overlap. The average uncertainty was found to be ±0.4m/s which is small compared to the average velocity through the passage of 14 m/s. The correlation value was about 0.6, and this was the value recommended by the software's manufacturer. The final resolution was 1 velocity vector/mm.

3.4.1 Data Acquisition Timing

The IOTA One solenoid valve driver was used as a trigger to control the data capturing, syncing the cameras with the pulsing so that the ensemble average taken with respect to the pulsing could later be found. A signal from the IOTA One would start the recording of the SPIV data using the PTU clock. A diagram that depicts this sequence is shown in Figure 14. Unfortunately, there can be minor differences in the exact timing of the triggering (see Run A and B).

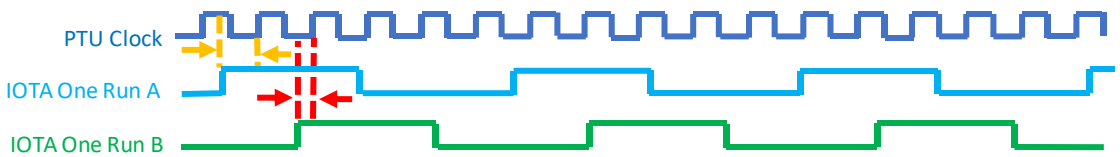

Figure 14: Timing of pulsed jet cases.

Since the data acquisition starts after receiving the signal from the IOTA One, there is potential for error between sets at the same frequencies. This error was a maximum of one phase of the PTU clock for each of the phase locked, or pulsed cases. This corresponds to an error between15.4 ms and 45.5 ms. The timing conditions for each of the standard cases was based on acquiring roughly 5000 images and taken at around 2.5kHz. All of these conditions including the maximum error is given in Table 5.

Table 5: Timing calculations for different pulsing frequencies.

f_{jet} (Hz)	F^+	F_{laser} (kHz)	T_{jet}(ms)	T_{laser}(ms)	# Phases	Phase Length (ms)	Max error (Phases)
Baseline	Baseline	2.47	NA	0.405	NA	NA	NA
16	0.29	2.496	62.5	0.401	156	0.401	1
19	0.35	2.489	52.6	0.402	131	0.402	1
22	0.40	2.486	45.5	0.402	112	0.406	1
45	0.82	2.475	22.2	0.404	55	0.404	1
65	1.19	2.47	15.4	0.405	38	0.405	1
70	1.28	2.45	14.3	0.408	35	0.409	1

4. Results

4.1 100k Baseline (no endwall pulsing)

The first goal was to establish a solid understanding of the baseline flow with the L2F blades in the linear cascade. A characterization of the baseline flow would then allow for a clear effect of the pulsed jets on the flow to be determined. The focus of this research was to study the passage vortex; and how it moves and changes in strength with time. The PV was selected because previous research showed that its interaction with the flow near the suction surface is responsible for much of the loss that is produced in the endwall region. Gross et al. found computationally that the PV intermittently lost its coherence with time, however, the time scales have not been fully determined experimentally [10]. Veley et al. used surface hot-films sensors to determine the fluctuations at these frequencies, however, without PIV data it could not be determined if those frequencies were from the PV bursting, flow oscillations, or other flow phenomena [15].

The SPIV velocity measurements were used to locate the PV position and strength. The Q-criterion (Q) was used to determine the location and measure the strength of the vortex with time. Q is the difference between the vorticity at a specific location and the shear strain rate [23]. Q in the velocity measurement plane was calculated using Equation 9, with the assumption of incompressible two-dimensional flow [24].

$$Q = \frac{\partial u}{\partial x}\frac{\partial v}{\partial y} - \frac{\partial u}{\partial y}\frac{\partial v}{\partial x} \quad \textbf{(9)}$$

Figure 15 shows the time averaged Q value for the baseline flow condition. The large vortex located between 0.22 y⁄C_x and 0.36 y⁄$C_{x,}$ is the PV. The vortex is elongated in the pitchwise direction; however, this was due to the vortex oscillating between two locations and spreading the average value. There was not a large spread in the spanwise direction because the vortex stayed at roughly the same location spanwise for most points in time. There was also a smaller, much weaker vortex present in the flow at 0.14 y⁄C_x. This vortex was below the secondary shear layer, and between the passage vortex and the suction side flow.

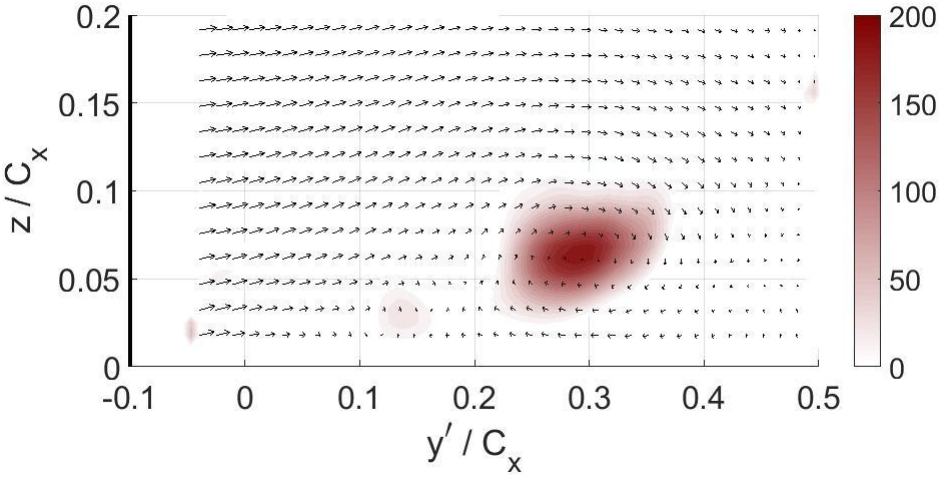

Figure 15: Time averaged Q for the baseline flow condition.

The major goal of the baseline flow investigation was to characterize how the PV strength and location changed with time. Therefore, the vortex core was found utilizing Q. The core was established to be the location in the flow where Q peaked, denoted by Q_p. The mean Q_p was found for the entire data set. The ratio of the instantaneous Q_p to the mean Q_p was then found. The first ten convective times are shown by the blue line in Figure 16. The core location in the pitchwise direction for each corresponding point is shown by the red line in Figure 16. Three large events are shown. These large events corresponded to major reductions in strength and change in position. These events are labeled A, B, and C and occurred at time scales between $1.9 < \Delta T+ < 6.7$ convective times. It was also clear the peak Q varied over eighty percent of the maximum peak Q during the ten convective times that were plotted. The pitchwise position also shifted about twenty percent of the overall axial chord during this time period. All these events corresponded to the rapid increase in vortex strength and the core location shifting towards the pressure side followed by a drastic decrease in strength and position shifting closer to the suction surface.

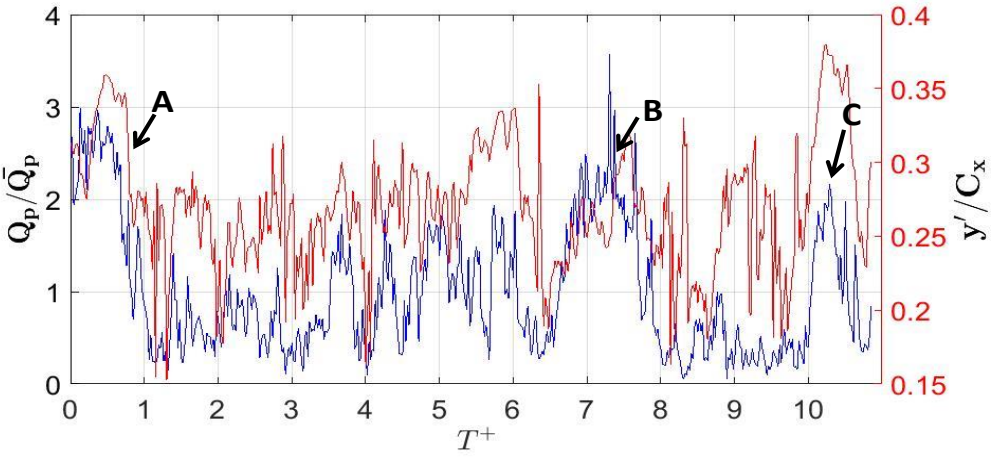

Figure 16: Peak Q ratio and the pitchwise location over ten convective times.

Figure 17 shows the same data set with a focus on the first five convective times. This plot focuses on the change in strength and core location for the time between events A and B in Figure 16. There were smaller events that occurred between the larger events and these are labeled t_a, t_b, t_c, and t_d. At time t_a, the PV was at its maximum strength of about 2.7 times the value of the average peak Q and was located close to the pressure surface at 0.33y/C_x. At time t_b, the strength of the core shifted to around a quarter of the peak strength that the PV had at time t_a and roughly 15% C_x towards the suction surface. Between events t_b and t_d, the PV strength and core location fluctuated at 25% of the strength at t_a and shifted 15% of the axial chord.

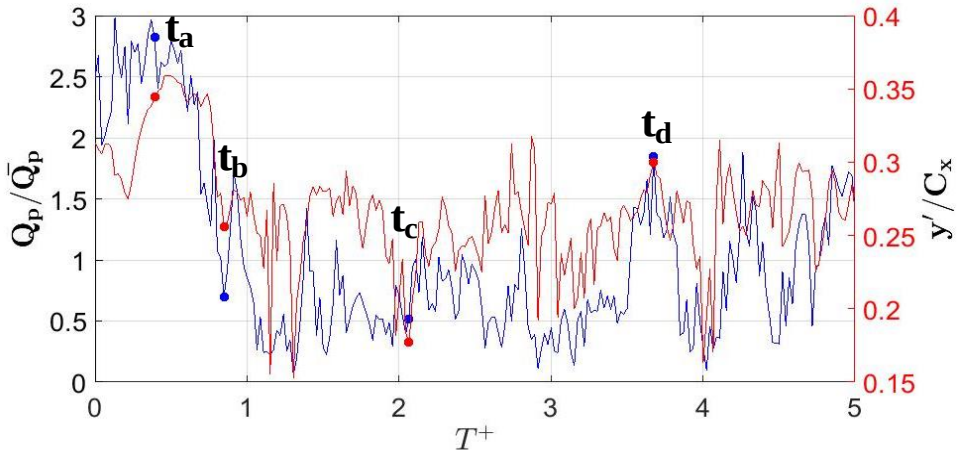

Figure 17: Peak Q ratio and the pitchwise location over five convective times.

The instantaneous values of Q for the entire flow field in the SPIV plane that were labeled as t_{a-d}, are shown in Figure 18. All the figures are shown on the same scales for easy comparison. From Figure 18a, it is clear that the PV was coherent, strong, and located close to the pressure side of the blade. The vortex was centered at 0.35 y/C_x and the Q strength was about 1000. In Figure 18b, the vortex was less coherent and was located closer to the suction surface at 0.25 y/C_x. At t_c (Figure 18c), the PV was dissipated and had lost

its coherence. Figure 18d showed that at time t_d the PV had gained some of its coherence back and was now located closer to the pressure side. Although, the PV was not as close to the pressure side as time t_a and is located at 0.3 y/C_x.

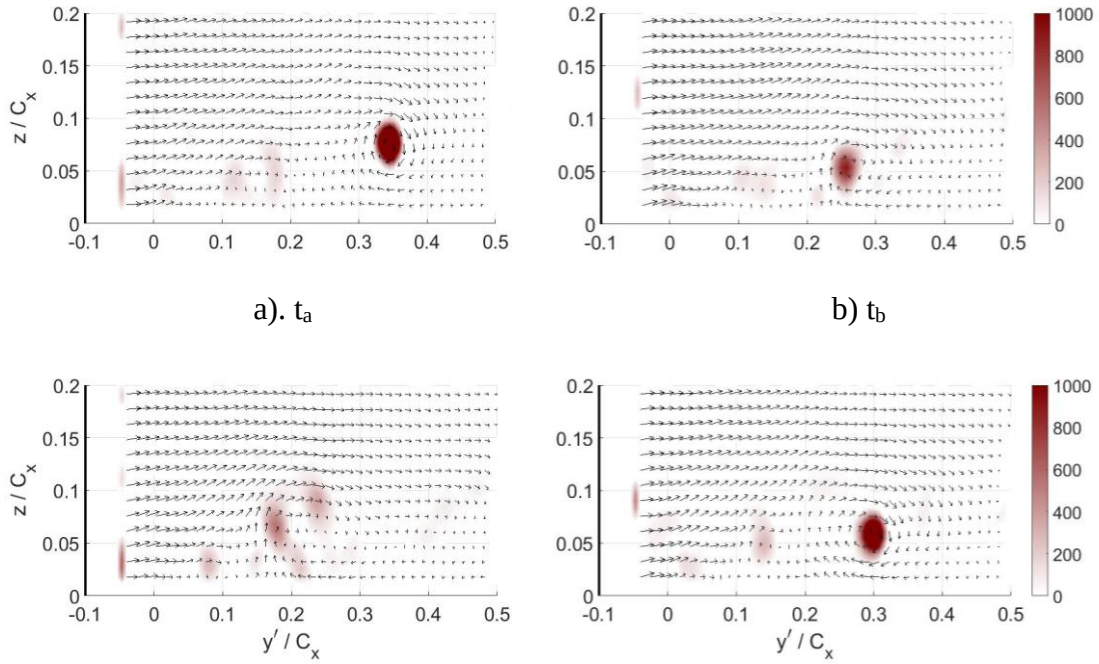

a). t_a b) t_b

c). t_c d). t_d

Figure 18: Four instantaneous plots of Q for the baseline flow.

In order to determine the frequencies at which the PV and other flow features oscillate, the frequency spectrum of Q was calculated using the SPIV data. The Fast Fourier Transform method was used to calculate the spectrum at all points in the field. The results of the power spectral densities were plotted to determine the frequencies at which significant peaks in the flow occur. Figure 19 shows the magnitude of the $F^+ = 0.4$ (f = 22 Hz) and this was the frequency that showed the largest peak in the frequency spectrum results. These results agree with what Veley et al. found using hot-films placed on the endwall along the PV lift off line [15]. The peaks in the PSD of Q were the locations

between which the PV oscillated (0.25 y⁄C_x and 0.35 y⁄C_x), meaning that the PV oscillations or undulation as described by Gross et al. occurred at a rate of 22 Hz (F^+ = 0.4) [10].

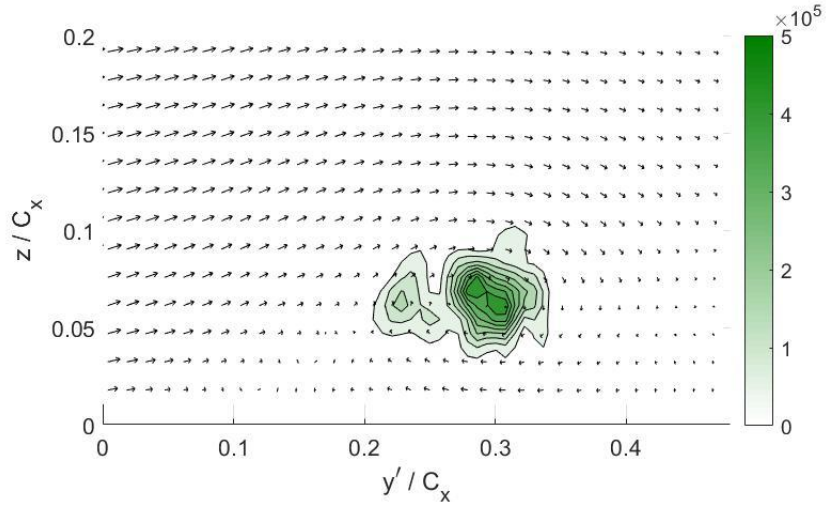

Figure 19: Magnitude of the PSD of F^+ = 0.4 frequency for baseline flow.

Turbulent kinetic energy (TKE) is a measure of the fluctuations that occur in the flow field. The equation for the TKE is given in Equation 10.

$$TKE = \frac{1}{2}(\overline{(u')^2} + \overline{(v')^2} + \overline{(w')^2}) \quad \textbf{(10)}$$

The velocity at an instance of time is equal to the sum of the mean velocity and the velocity perturbation, Equation 11.

$$u = \bar{u} + u' \quad \textbf{(11)}$$

The mean TKE was calculated for the baseline flow condition, Figure 20. The maximum TKE was located between 0.25 y⁄C_x and 0.35 y⁄C_x. These is the same location as the PV in the Q plot shown in Figure 15. The vortex oscillated in this region results in more fluctuations in this region than in the overall flow field.

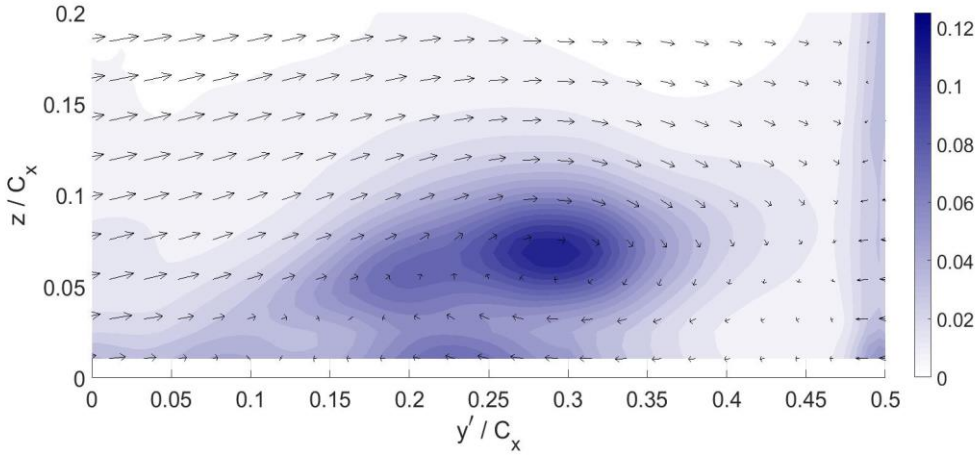

Figure 20: TKE of the mean flow for the baseline flow at 100k.

Another measure of the strength of a vortex is circulation. The circulation is the strength of the rotation of a vortex. Unlike Q, however, it gives a single value that is representative of the entire vortex strength and does not provide a way to visualize a vortex. If the circulation of a vortex is positive, then the vortex is rotating in the clockwise direction and if the circulation is negative then it is rotating in the counterclockwise direction. The circulation is equivalent to the line integral of the velocity over the closed contour surrounding the core of the vortex, Equation 12.

$$\Gamma = \oint_c \vec{V} \cdot d\vec{l} \tag{12}$$

Stokes theorem relates a line integral to an area integral. This theorem can be used to turn an area integral into a line integral or vis versa as shown in Equation 13.

$$\oint_c \vec{F} \cdot d\vec{s} = \iint_A \nabla \times \vec{F} \cdot dA \tag{13}$$

The vorticity is related to velocity through the curl operation Equation 14.

$$\vec{\omega} = \nabla \times \vec{V} \tag{14}$$

By combining this relation with the Stokes relationship, Equation 13, the circulation can be found by using Equation 15.

$$\Gamma = \iint_A \vec{\omega} \cdot dA \tag{15}$$

The equation for circulation can be further simplified since the vorticity is dominate in the out of plane direction, and this is shown in Equation 16, where z is the out of plane direction and A lies in the SPIV plane.

$$\Gamma = \iint_A \omega_z \cdot dA \tag{16}$$

Since there is no overall governing equation for the flow field, the fluctuations of the circulation had to be calculated numerically. The first step in calculating the PV's circulation was to isolate the PV at each point in time. This was done utilizing Q. An example of the non-isolated PV and the area surrounding it are given in Figure 21.

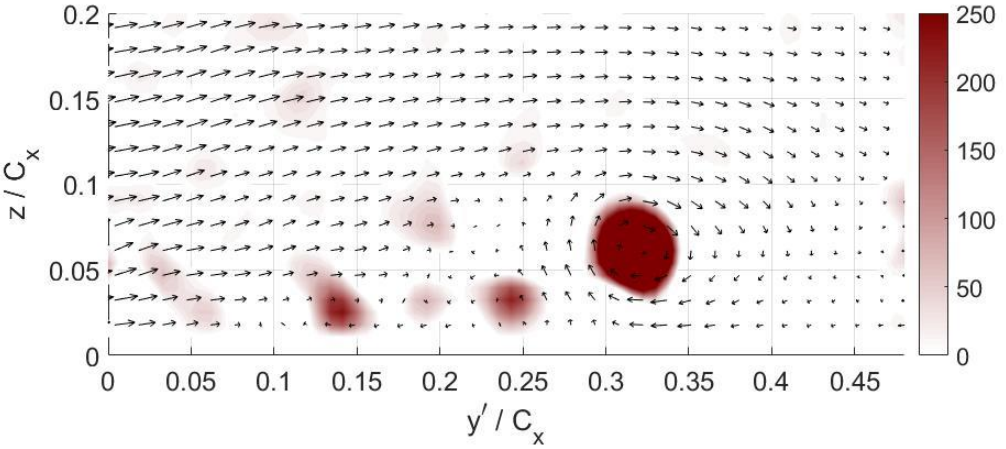

Figure 21: Full value of Q surrounding the PV for the baseline flow.

To isolate the PV a threshold of 500 was set for the Q_{max} value. If the instantaneous Q_{max} was less than 500 all of the values of Q were set to zero. At those times the PV was incoherent or dissipated at that point in time. After that the threshold was set based off the

maximum value of Q at a given point in time. If the value of Q at any point in the flow field was less than ten percent of the Q_{max}, then the Q at that point was set to zero. This was the same cutoff value that Gross et al. used to isolate the vortex bounds [25]. The final isolated PV is shown in Figure 22.

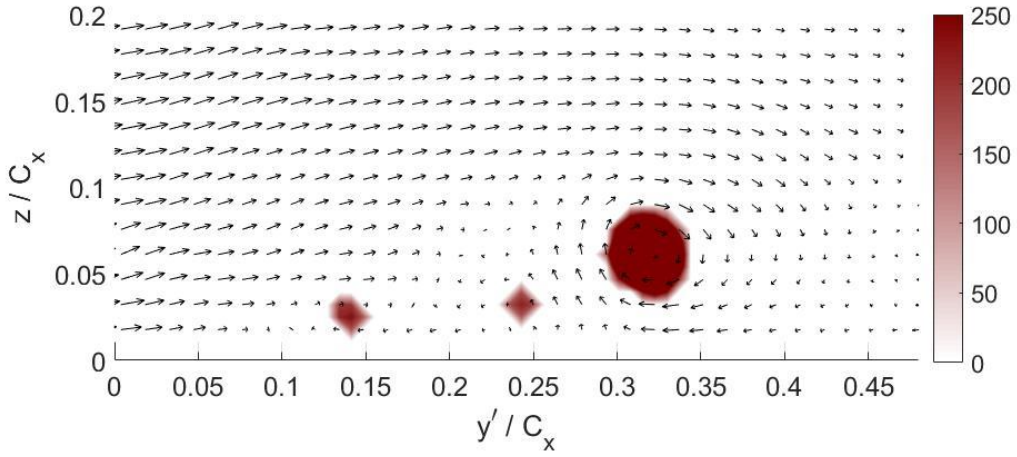

Figure 22: Q values for isolated vortex for the baseline flow.

The next step was to find the core of the isolated vortex, by limiting the search window to the approximate area that encases the PV. This step ensured the core value would be for the PV and not some other point in the field of investigation. A box was created around the core of the PV. The box extended ten points in each direction of the core, or to the edge of the SPIV region if that was within ten. The corresponding vorticity for each point was then calculated and multiplied by its corresponding area. If the corresponding vorticity was positive the value was not valid. Previously, the velocity vectors showed the PV rotation was counterclockwise, so if the vorticity at a point was clockwise the PV was not coherent, meaning the value did not correspond to the PV. The sum of all these values was then found to get the overall circulation of the PV.

The PV circulation was calculated for each point in time. The circulation for the first eleven convective times is shown in Figure 23. From this plot, the vortex changed in strength with respect to time and confirms the results found from Q.

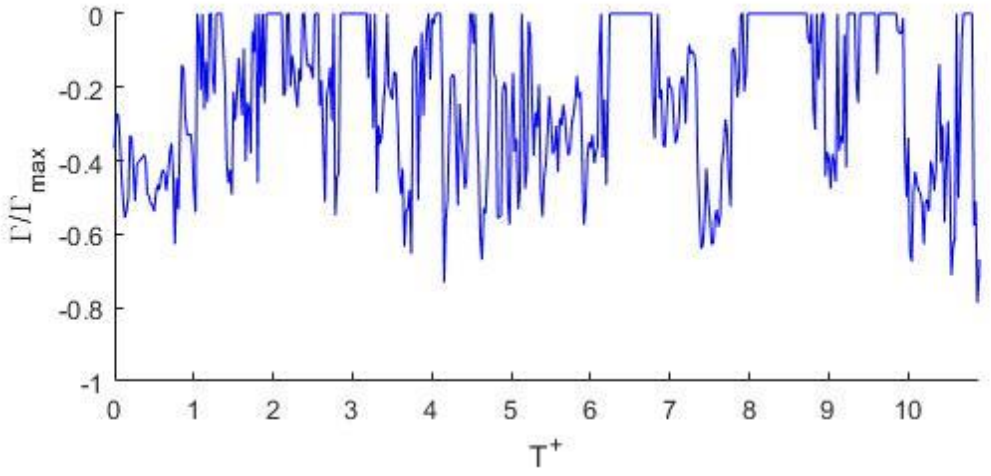

Figure 23: Baseline circulation for ten convective times.

Figure 24 shows the circulation for the five convective times of the data set. This makes it clearer that the PV lost its strength at extremely rapid rates, on the order of milliseconds.

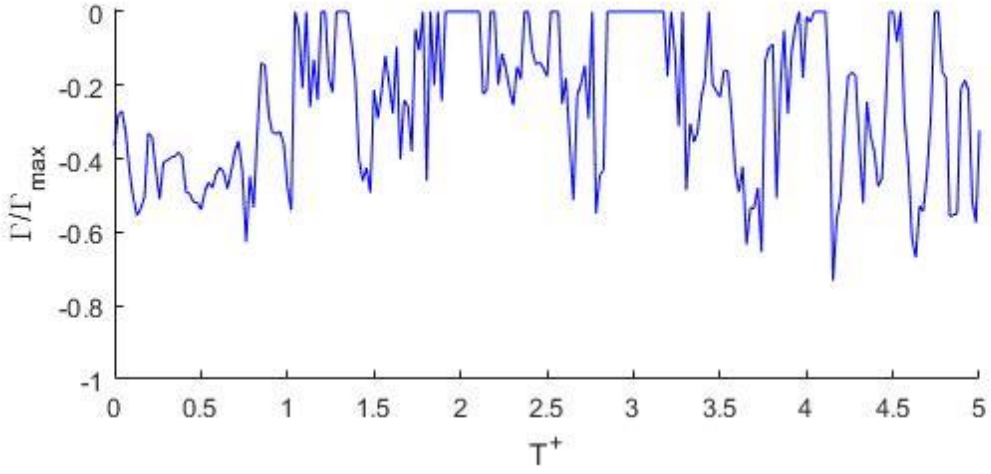

Figure 24: Baseline circulation for five convective times.

4.2 TKE for $F^+ = 0.4$ and $F^+ = 1.2$ pulsed cases

One way to see the effects of the jets was to use the TKE. The mean TKE was calculated for both the $F^+ = 0.4$ and $F^+ = 1.2$ jet pulsing cases. These results were calculated utilizing the slow repetition data, which was taken at 100 Hz rather than about 2.5 kHz with 5000 image pairs. It was taken at a slower rate to span a greater time so that the results accurately express the mean for the overall flow. The results for the $F^+ = 0.4$ pulsing case is shown in Figure 25. It is clear the pulsed jets reduced the TKE for the overall flow field, particularly the PV. The passage vortex was now located closer to the suction surface centered at roughly 0.2 y/C_x. There was also an increase in TKE located near the region where the jets would be passing through the SPIV plane, as the jets are upstream of the plane, at 0.45 y/C_x. This was expected since the jets were injecting air into the flow that would be interrupting the typical flow through the passage in that region.

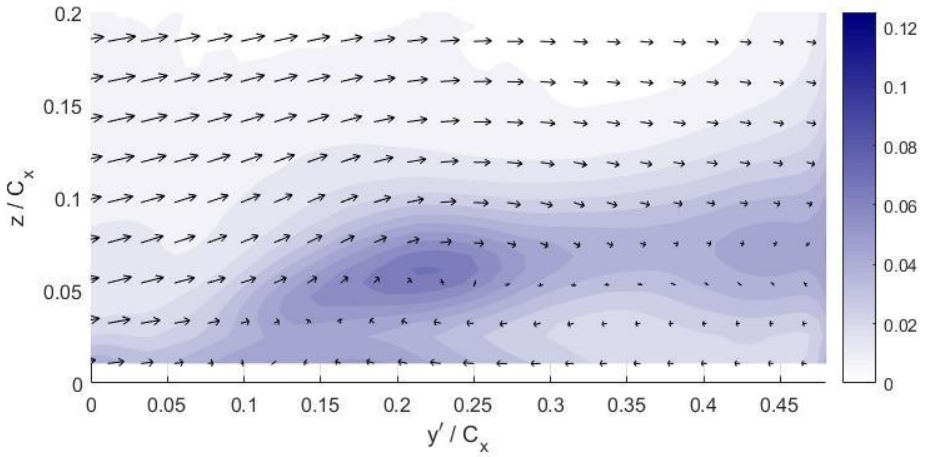

Figure 25: Mean TKE for the $F^+ = 0.4$ pulsing case.

Figure 26 shows the time averaged TKE for the $F^+ = 1.2$ pulsing case. At the higher pulsing frequency, the TKE was lower than the $F^+ = 0.4$ pulsing case. Meaning the flow had even weaker velocity fluctuations. The oscillations, however, from the jet core were

now shifted closer to the suction surface at roughly 0.175 y/C_x. There was still higher turbulence near where the jet would pass through the plane located near 0.45 y/C_x. It extended higher in the spanwise direction, implying the jets penetrated the flow more at that frequency.

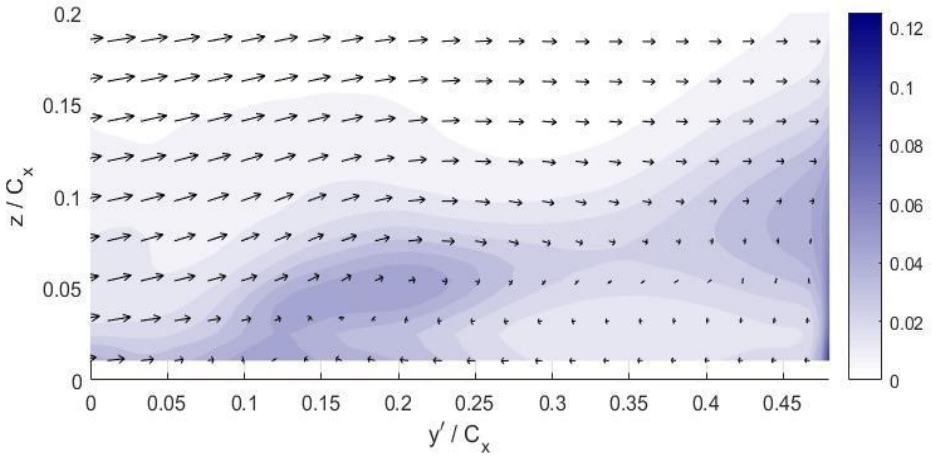

Figure 26: Mean TKE for the F^+ = 1.2 pulsing case.

The TKE was also calculated at each phase using the high-speed measurements. This was accomplished by finding the phase mean of the flow field. The data needed to be broken down into individual phases. Longer data sets were taken for the F^+ = 0.4 and F^+ = 1.2 pulsing cases to ensure that the number of ensembles necessary were captured. For the data presented in Figure 27, 24,992 image pairs were captured at a rate of 2.486 kHz. Meaning at the F^+ = 0.4 (22 Hz) jet pulsing frequency there were 113 phases per pulsing period with 221 ensembles or averages per phase. Figure 27 shows four different phases evenly spaced across the pulsing period. From these plots it is clear the amount of TKE present per phase was time dependent. The phase average TKE gives an indication of the time the jet began firing. At the start of the period the PV was relatively stable. The PV was less stable or coherent a quarter of the way through the period. The PV gained some

stability as the jet passed halfway through the period, at phase 57 (Figure 27c). The jet stayed on or the remnants of it can be see passing through the SPIV plane three-quarters of the way through the period, until it turned off at roughly phase 104. The jet was present in the SPIV plane for 42% of the pulsing period. This was comparable to the input duty cycle on the IOTA One solenoid valve driver of 45%.

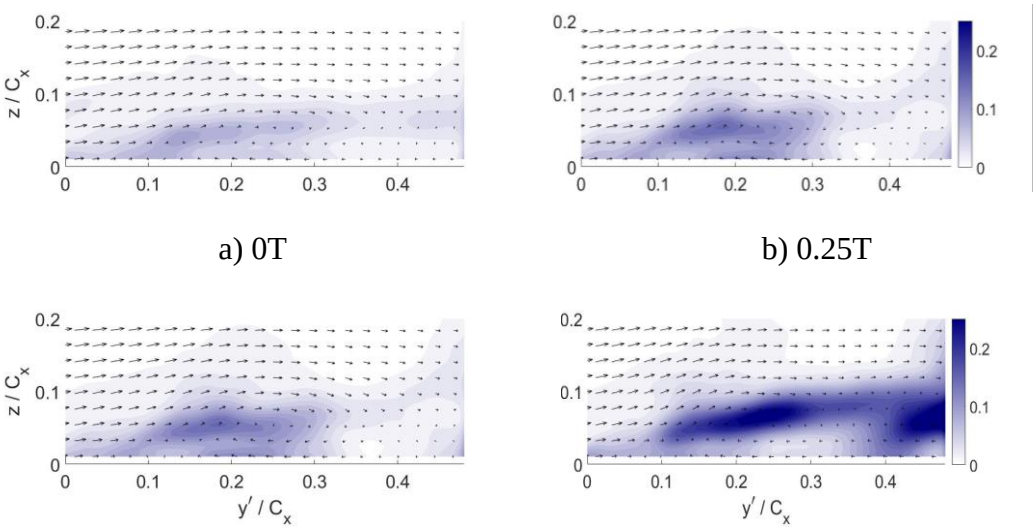

a) 0T b) 0.25T

c) 0.5T d) 0.75T

Figure 27: Snapshots of the phase averaged TKE for the F^+ = 0.4 pulsing

Figure 28 shows the phase averaged TKE for four instantaneous points in the pulsing period for the F^+ = 1.2 (65 Hz) pulsing case. In this data set there were 24960 images pairs captured at a rate of 2.47 kHz, meaning there were 38 phases for pulsing period with 656 ensembles or averages per phase. Like in Figure 27, it is clear in Figure 28 that the TKE was phase dependent. The jet effects convected into the SPIV plane at phase 17 (0.45T) and turned off at phase 33 (0.89T). The jet was present in the flow field for 42% of the period. This result matched the measurements for the F^+ = 0.4 pulsing case.

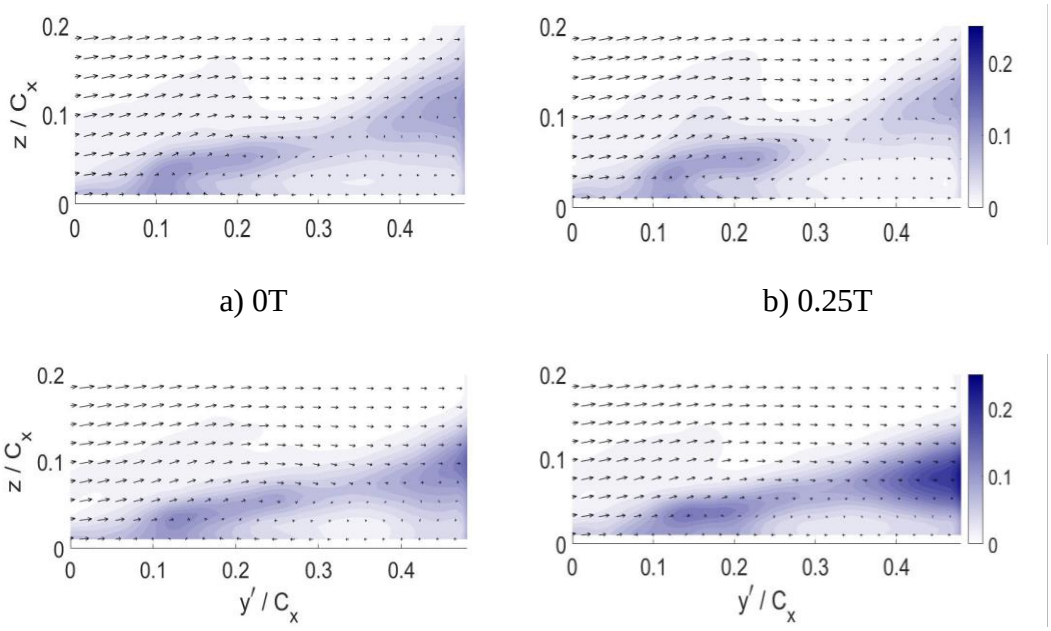

a) 0T b) 0.25T

c)0.5T d)0.75T

Figure 28: Snapshots of the phase averaged TKE for the F^+ = 1.2 pulsing

4.3 Q-criterion and Position

The time average values for Q were calculated for both jet pulsing cases. The data taken at 100 Hz was used to calculate these averages. The F^+ = 0.4 pulsing case is shown in Figure 29. It is clear that the PV shifted towards the suction surface. The PV was located between 0.18 y'/C_x and 0.29 y'/C_x, meaning the PV had a smaller spread than in the baseline case. By combining this knowledge with the weaker turbulent kinetic energy, the PV experienced smaller oscillations than for the no pulsing baseline case. Also, the small vortex in the baseline flow was no longer present. Overall, the PV was weaker than the baseline case. There was also a second vortex present in the pulsing data located near where the jets passed through the flow field in the turbulent kinetic energy plot. This second vortex is much weaker than the PV meaning it either is actually much weaker than the PV or it is not present at all points in time in the flow.

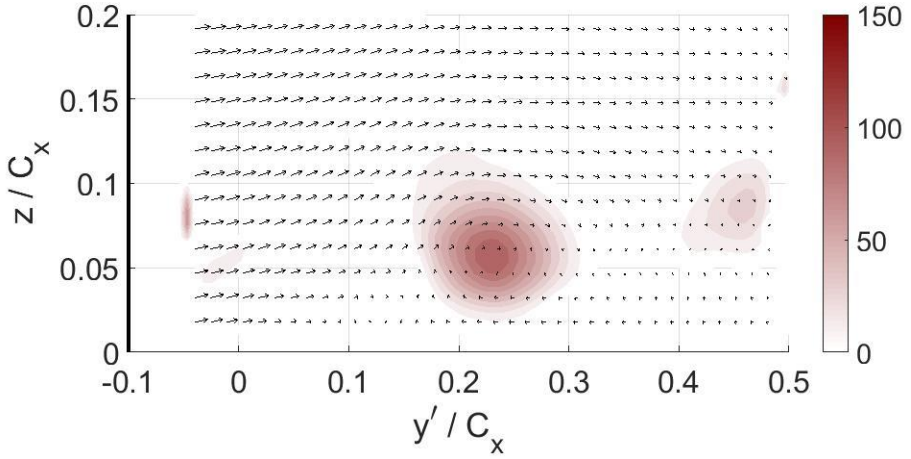

Figure 29: Time averaged Q for the F^+ = 0.4 pulsing case.

In Figure 30, the time average value of Q for the F^+ = 1.2 pulsing case is shown. The PV dominates the flow in the region of interest. When compared to Q for the baseline flow and the F^+ = 0.4 pulsing case, the PV was shifted closer to the suction side of the blade between 0.16 y'/C_x and 0.26 y'/C_x. Therefore, the passage vortex had less spread in position than it did in the other cases. When combined with the TKE, the vortex oscillated even less than the F^+ = 0.4 pulsing case and much less than the baseline. The PV strength was also lower than in either of the two previous cases.

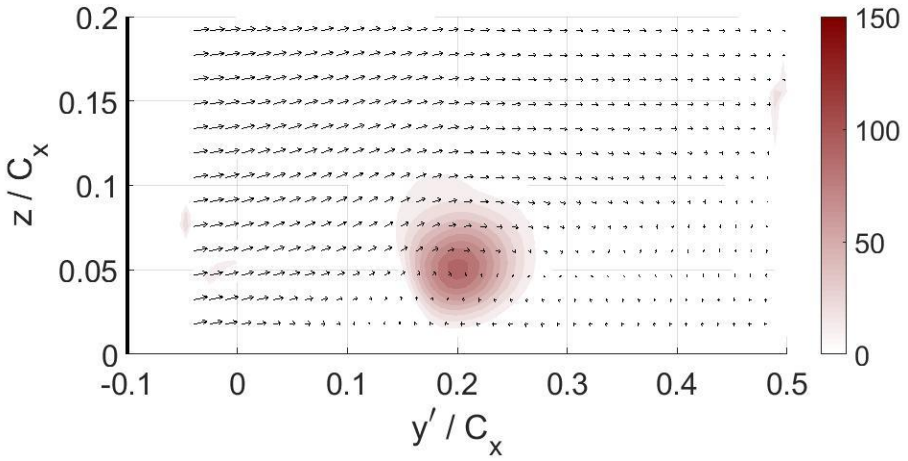

Figure 30: Mean Q for the F^+ = 1.2 pulsing case.

Figure 31 shows the time averaged Q value for the baseline, $F^+ = 0.4$ and $F^+ = 1.2$ endwall pulsing overlaid. Clearly, the endwall jets shifted and weakened the PV. The pulsed jets shifted the PV closer to the suction surface. With $F^+ = 1.2$ closest to the suction surface. The PV was also weakest for $F^+ = 1.2$. For both pulsing cases the second vortex beneath the secondary shear layer was eliminated.

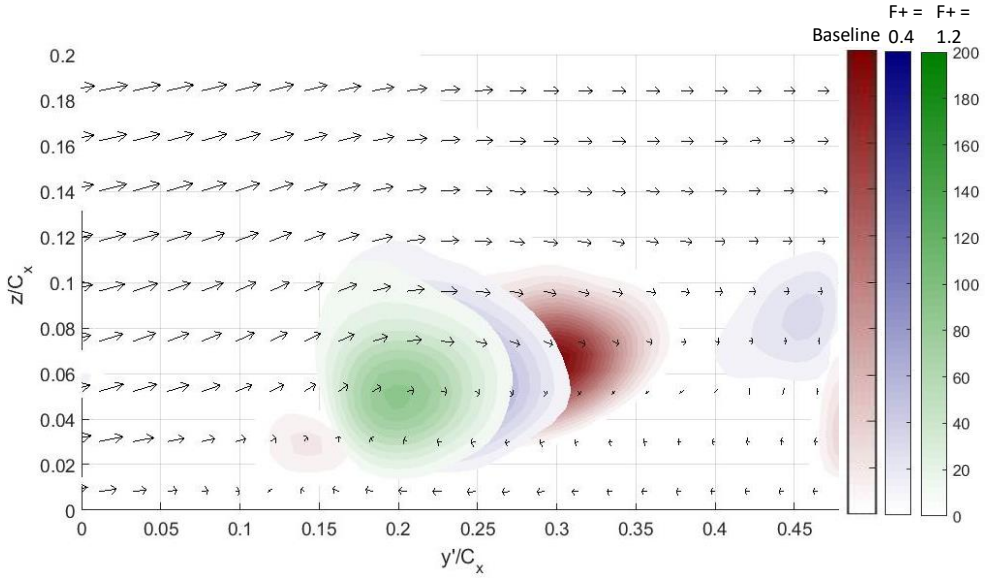

Figure 31: Q values for the baseline, F+ = 0.4 and F+ = 1.2 pulsing cases.

The phase average of Q was calculated for both pulsing cases. The data sets with roughly 25000 image pairs were utilized to calculate these averages. Figure 32 shows Q at different phases in the pulsing period. At the start of the period, Figure 32a, the PV was not entirely coherent and relatively weak. The PV at this point in time was also located at 0.22 y'/C_x. A quarter of the period, Figure 32b, the passage vortex was located closer to the pressure surface and centered at 0.25 y'/C_x. The passage vortex was more coherent, or stronger than it was in the beginning of the period. Halfway through the period no coherent PV is visible. It appears to have broken down and spread out into many smaller weaker vortices. The vortices appeared to be in a random pattern with little predictability. When

combined with TKE data at this period, it is clearly showing an unsteady breakdown of the PV. Three quarters of the period, the PV has either split in half or a second vortex has formed. This was the time the jet was passing through the flow. The original part of the PV has now shifted closer to the suction surface and regained some of its strength. It was not nearly as strong as it was at the quarter period. Therefore, the PV was coherent and the only dominate flow feature in the plane when it was located closest to the pressure side. The PV was weaker when it was closer to the suction side. When there were two vortices in the flow field the original PV gained strength as it moved towards the suction side and the second vortex gained strength as it moved towards the pressure surface.

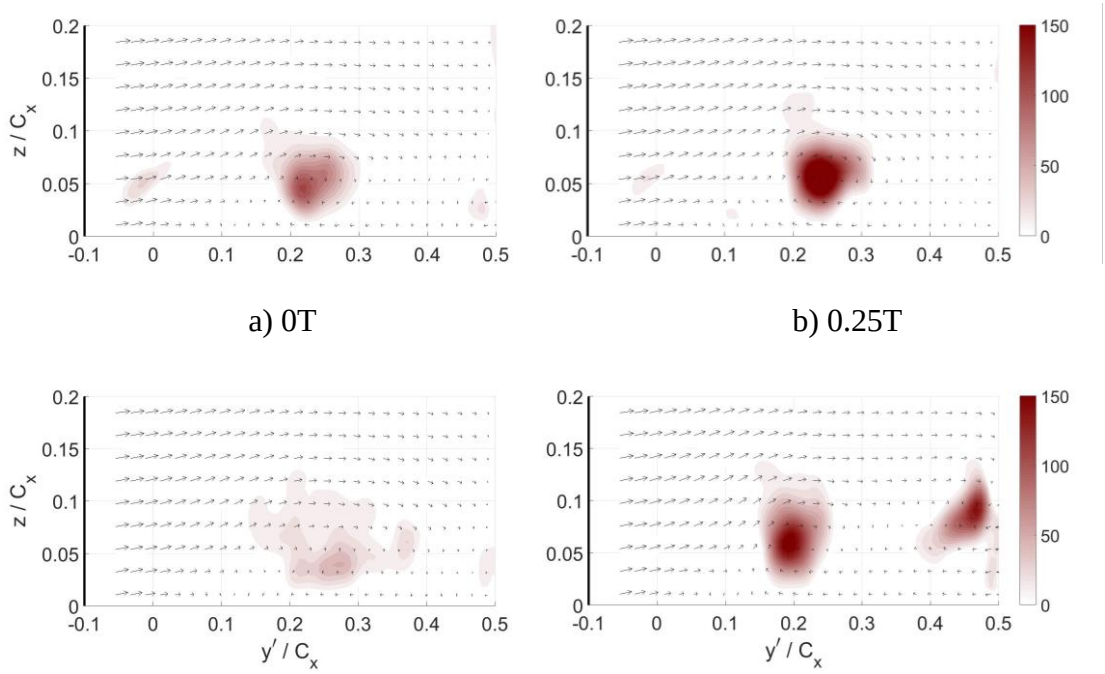

a) 0T b) 0.25T

c) 0.5T d) 0.75T

Figure 32: Values of Q throughout the period for the F^+ = 0.4 pulsing case.

Figure 33 shows the phase averages of Q at four points in time through the pulsing period for the F^+ = 1.2. At the start of the period, Figure 33a, the PV was located close to

the suction surface at 0.23 y'/C_x and was not fully coherent (i.e. the PV was weak). The PV was closer to the suction surface than it was at the start of the pulsing period for the F^+ = 0.4, however, it was about the same strength. Figure 33b, like F^+ = 0.4, the PV had regained its coherence and strength and shifted closer to the pressure surface. However, it was not as close to the suction surface, as observed at lower frequencies, and was located

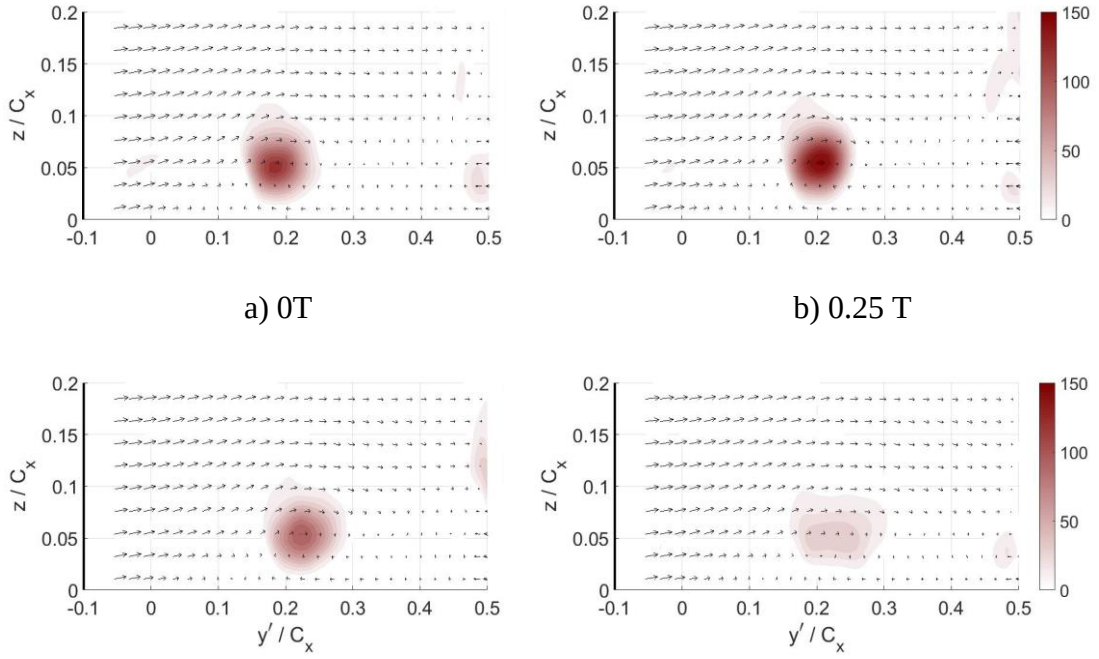

a) 0T b) 0.25 T

c) 0.5T d) 0.75T

Figure 33: Values of Q throughout the period for the F^+ = 1.2 pulsing case.

at 0.20 y'/C_x. Halfway through the pulsing period, the PV had lost its strength. The PV continued to lose its strength three quarters of the way through the period, however, no second vortex formed as in the F^+ = 0.4 case.

To determine how the location and strength of the PV changes over the pulsing period, the phase averaged peak location of Q and its pitchwise location was plotted over the entire pulsing period. For both pulsing cases, the data sets with almost 25000 image pairs were used to calculate these ensemble averages. The results for the F+ = 0.4 case is shown in

Figure 34. The passage vortex went through two cycles of gaining and losing strength per pulsing period. This confirmed what was shown in the results for the different time periods of the pulsing for the Q plots that was shown in Figure 32. The vortex gained strength and then rapidly lost strength when the vortex splits and then gained its strength again. The PV pitchwise location only went through one cycle of position change per pulsing period. Roughly halfway through the period the PV rapidly shifted toward the suction surface. Also, the strength of the vortex varied 80% over the pulsing period and the pitchwise location of the core varied 13% of the axial chord over the period.

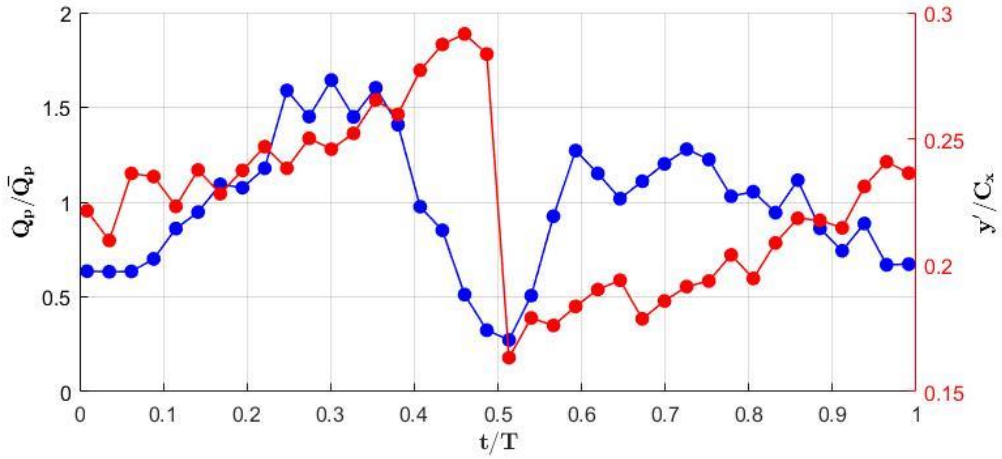

Figure 34: Peak Q Ratio and Pitchwise location for one pulsing period for F^+ = 0.4 pulsing case.

Figure 35 shows how the PV strength and position varied over one pulsing period for the F^+ = 1.2 pulsing case. The peak strength, or core strength, of the PV varied over 75% of the max value. It went through one cycle of gaining and losing strength. This was different than the F^+ = 0.4 case, where the PV underwent two cycles of gaining and losing strength. The results from Q plots, Figure 33, confirmed the vortex did not go through two cycles of changes in strength, since the PV did not spilt as in the F^+ = 0.4 case. The pitchwise location of the PV also changed less than both the baseline and F^+ = 0.4 case, as it varied by 7% of

the axial chord over the period. The pitchwise location went through one major cycle of change in position. Halfway through the pulsing period, the PV did shift slightly to the suction surface and then back towards the pressure surface, however, this was not a large change in position. This change was only about 3% of the overall axial chord.

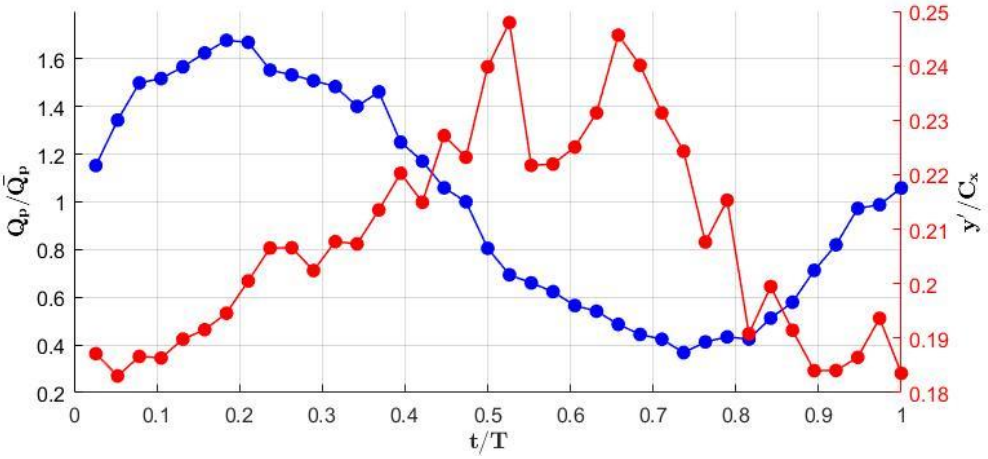

Figure 36: Peak Q Ratio and Pitchwise location for one pulsing period for F^+ = 1.2 pulsing case.

The phase averaged TKE gave insight into the amount of fluctuations present in the flow field, however, it did not physically quantify the amount the PV position fluctuated. One way to quantify that value is by calculating the mean absolute deviation, Equation 17.

$$MAD = \frac{1}{n}\sum_{i=1}^{n} |y' - \bar{y}'| \tag{17}$$

The mean absolute deviation was calculated for the pitchwise position of the core for the passage vortex. The plot of this for the F^+ = 0.4 jet pulsing condition is given in Figure 37. The PV shift from the phase average location was dependent upon the phase. At the start of the pulsing period, the passage vortex did not fluctuate a great deal from its mean location. Roughly one the third of the way through the pulsing period the PV fluctuated the most from the phase mean location. At the maximum the PV pitchwise location varied a

total of 12% of the axial chord. After the jet passed (phase 57 of 0.5T), the PV continued to stabilize. Therefore, the pulsed endwall jets helped to stabilize the PV. Some of the variability shown could be due to the method that was used to locate the core of the PV. The core was established to be the location of the maximum Q, which means it most likely was not always located in the exact same relative spot of the PV. Since the PV typically had a width of about 10% axial chord this could make the fluctuations appear much larger and noisier they were in reality.

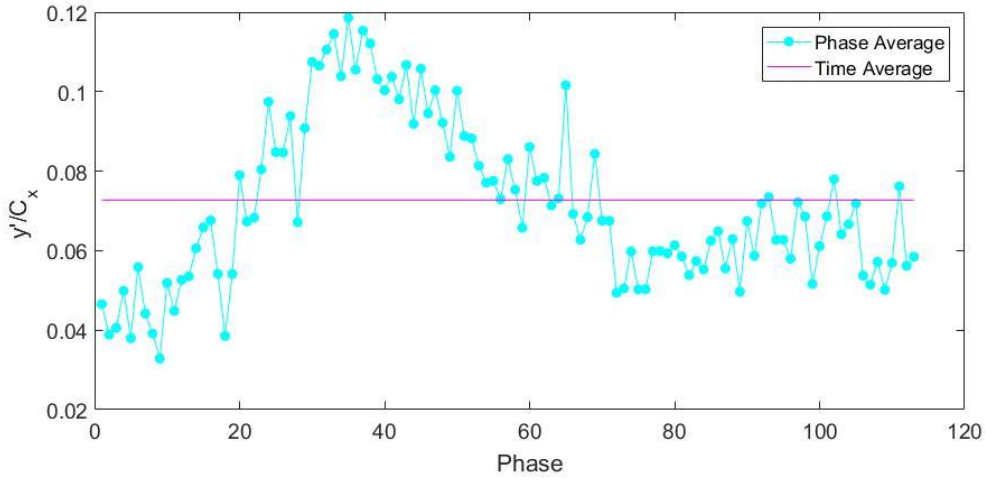

Figure 37: Mean absolute deviation of the pitchwise location for $F^+ = 0.4$ pulsing case.

The absolute average deviation for each phase for the $F^+ = 1.2$ case is shown in Figure 38. The overall mean absolute deviation was lower than the $F^+ = 0.4$ case. The difference in the mean absolute deviation for each phase, however, was much smaller. The range was only 4% axial chord, instead of 9% axial chord. The mean absolute deviation did change for each fluctuation of the pulsing period. It appeared to be in a cyclic nature over the period. For both frequencies, the mean absolute deviation underwent one large cycle over the period, however, there were smaller fluctuations throughout the larger overarching

cycle. At the start of the period, for the F^+ = 1.2 case, the mean absolute deviation was relatively high. It then decreased as the jet passed through at phase 15. Then it increased once the effects of the jet passed by at phase 35 where the average absolute deviation increased again.

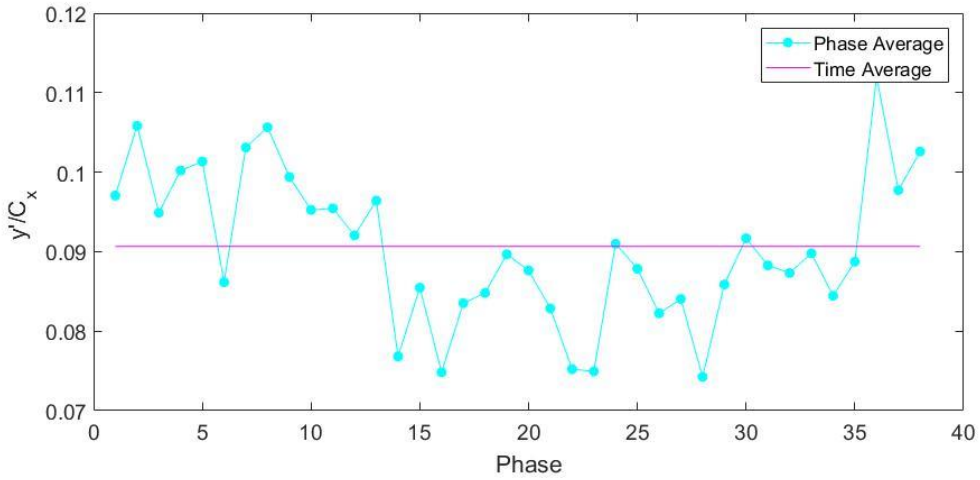

Figure 38: Mean absolute deviation of the pitchwise location for F^+ = 1.2 pulsing case.

Four other pulsing frequencies were tested; however, they were not investigated as closely as the F+ = 0.4 and 1.2 cases. The F+ = 0.4 pulsing frequencies was selected for detailed study because the natural oscillations of the passage vortex occurred at this frequency. F+ = 1.2 was selected because it was the frequency that corresponded with the maximum measured pressure loss reduction. The time average Q was calculated for the four additional pulsing frequencies F+ = 0.29, 0.34, 0.81 and 1.26. The maximum value of Q was then found for each nondimensional frequency. This value was used to represent the core of the passage vortex. At all pulsing frequencies, the endwall jets weakened the PV. It is also clear that the strength of the passage vortex changed with pulsing frequency,

but not a great deal. The vortex was weakest at the jet pulsing frequency of F+ = 1.26, however, it was not much stronger at F+ = 1.2.

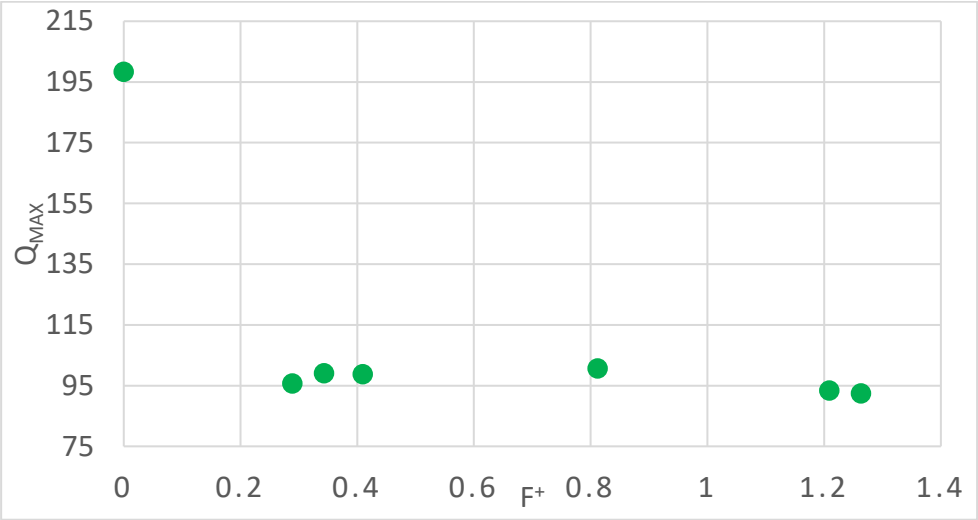

Figure 39: Maximum Q of the mean flow fields for all frequencies.

4.4 Circulation for baseline, F+ = 0.4, F+ = 1.2 at Reynolds = 100k

Q can be utilized to determine the strength and position of a vortex; however, circulation can be a more beneficial method of quantifying a vortex strength. Q gives a value at each point of the flow field. If the values are large and grouped together, it typically represents a vortex. Circulation, however, gives a single value for the entire vortex. Meaning, it represents the overall strength of the vortex in a single value. The ensemble averages of the circulations were calculated to determine how the strength of the PV changes over the course of the pulsing period. About 25000 image pairs were used to calculate the ensemble averages. The ensemble average of the circulation for the F+ = 0.4 case is given in Figure 40.

The PV undergoes only one cycle strength changes per pulsing period, which is different than using peak Q. The PV circulation started out low and then gained strength

until roughly 30% of the way through the period. This agreed with the analysis using peak Q that were given in Figure 16. The passage vortex then rapidly lost its strength again, but at a slower rate than it gained its strength. The difference between the number of cycles that the strength underwent for the Q and circulation, are mostly likely due to the different methods by which the values were calculated. The peak Q would represent the PV as being strong if there was a single point in the vortex that was large. To be strong according to the circulation result, the vorticity would need to be large for many different points surrounding the core.

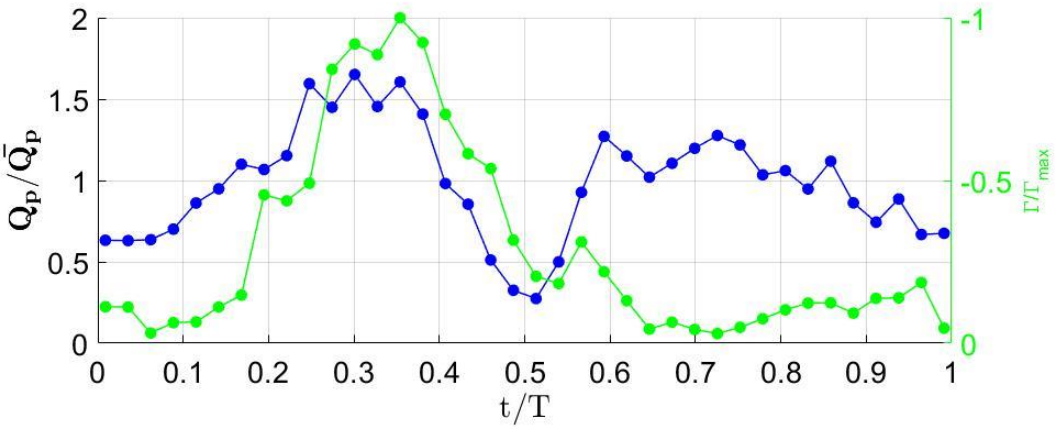

Figure 40: Phase average of Circulation for F^+ = 0.4 pulsing case.

The circulation over a single pulsing period for the F^+ = 1.2 case is given in Figure 41. Like for the F^+ = 0.4 case, the circulation of the PV changed over the course of the pulsing period. The PV had a maximum strength roughly 40% of the way through the pulsing period instead of 30% like the F+ = 0.4 pulsing case. The circulation demonstrates that the PV underwent through one cycle of gaining and decreasing strength over the pulsing period. This is consistent with the results from the peak Q, Figure 36, but the time of maximum strength did not match the results from the peak Q. The peak Q maximum

strength occurred at 20% of the period not 40%. This could be due to the fact the peak Q only accounted for a single point in the mean PV, whereas the circulation accounted for the entire strength of the PV.

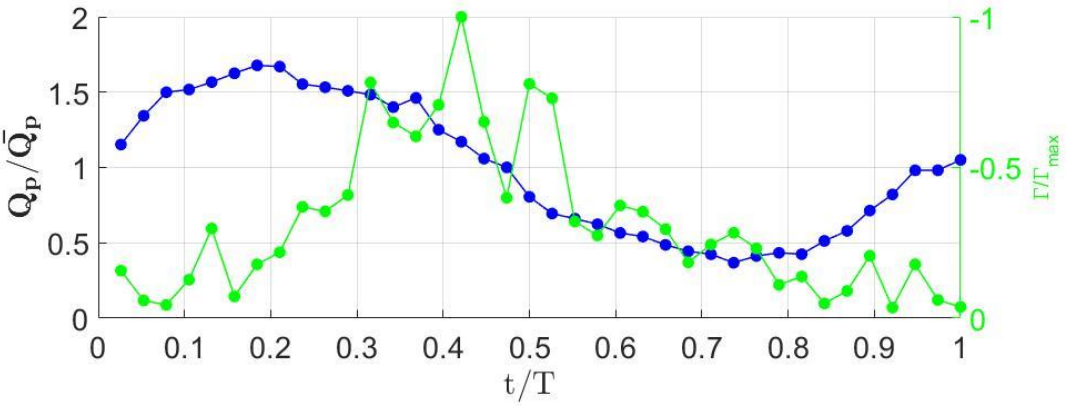

Figure 41: Phase average of Circulation for F^+ = 1.2 pulsing case.

Figure 42 shows the mean circulation for the baseline and all pulsing cases. This plot clearly demonstrates that the circulation, which can be used as a representation of strength, was dependent upon the pulsing frequency of the endwall jets. Also, all the pulsing frequencies reduced the strength of the PV by at least 60% from the baseline 100k flow condition. The maximum reduction in the magnitude of the circulation of the PV occurred at an endwall jet pulsing frequency of F^+ = 1.2. At this frequency the circulation had a strength of -0.000506 which corresponds to a strength reduction of 98.7% compared to the baseline circulation.

In general, as the pulsing frequency increased the magnitude of the circulation decreased. Therefore, the PV strength decreased which agreed with the results using Q. This was not true at a pulsing frequency of F+ = 1.24, where the magnitude of the circulation increased. Meaning the PV had regained some of its strength. Also, the

magnitude of the strength of the circulation also increased slightly at $F^+ = 0.34$, however, it decreases again at $F^+ = 0.4$. The general trend of this figure matches the results for the total pressure loss reduction and the exit angle improvement. This reinforces the idea that the weakened PV is what led to the total pressure loss reduction and improvement in the exit angle or at least is part of why these improvements occur.

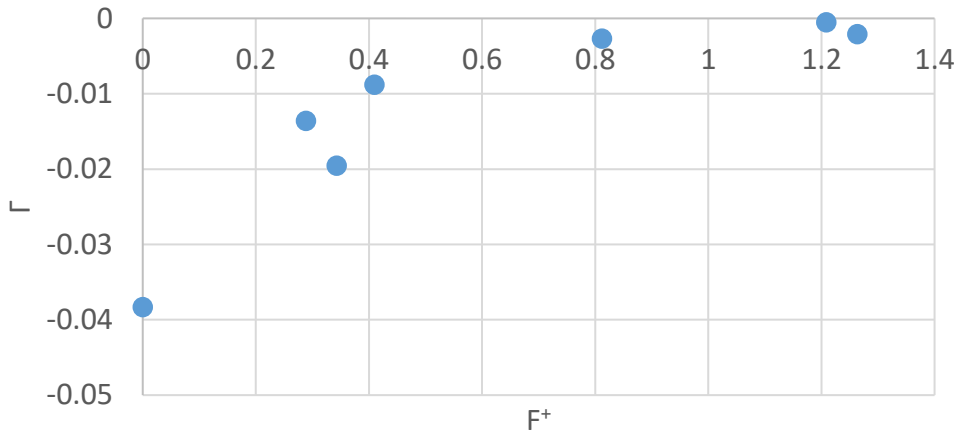

Figure 42: Mean circulation for each pulsing frequency.

4.5 Core location

To determine how the pulsing frequency influenced the location of the PV, the core locations were found utilizing both the Q criterion and the Gamma method. Figure 43 shows the results for the time average pitchwise location of the PV core calculated using Q. Only the pitchwise location was investigated because previous research showed the PV predominately moved in the pitchwise direction at a Reynolds number of 100k. It did not move much in the spanwise direction. The core location was defined as the location where Q was a maximum. These corresponding strengths for each of the frequencies can be found in Figure 39. This plot shows that as the pulsing frequency increases the PV moves closer to the suction surface until $F^+ = 1.2$ after which point the PV moves towards the pressure

surface. Similar to the strength of the PV, the core of the location determined by Q had a similar shape as the total pressure loss reduction and the exit angle improvement. This means that there was a correlation between the improvement in the loss reductions and the location of the PV with respect to the suction surface. Therefore, the closer the PV is to the suction surface the larger the improvement is in both the exit angle and total pressure loss reduction.

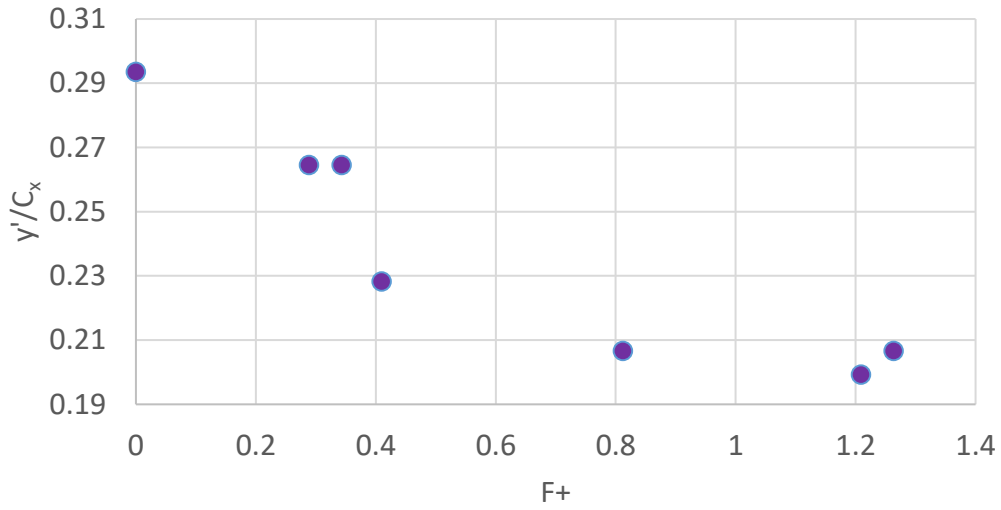

Figure 43: Pitchwise position of the core location for each pulsing frequency and baseline flow condition calculated using Q.

The core location of the PV in the pitchwise direction was also found using the Gamma method described in Graftieaux et al. [26]. This method is a way to identify a vortex without utilizing Q. The method relies solely on the topology of the velocity field. It does not account for the magnitude of the velocity field to determine the location of the PV. The equation to calculate Γ_1 which represents the location of the core of the PV is given in Equation 18.

$$\Gamma_1(P) = \frac{1}{k}\sum_{R}\frac{\left(PM\Lambda\vec{U}\right)\cdot\hat{z}}{||PM||\cdot\left|\left|\vec{U}\right|\right|} = \frac{1}{k}\sum_{R}\sin(\theta) \quad \textbf{(18)}$$

One parameter that was not expected to have a large effect on the results for Γ_1 is the window size defining region R, used to search for the location of the PV. This definition is given in Equation 19.

$$W = \sqrt{k} \quad \textbf{(19)}$$

A convergence analysis was completed to determine the window size that would be necessary to get an accurate result for the location of core of the PV. The results from the convergence analysis are given in Figure 44. From this analysis it was determined that a window size of 11 points would be suitable. With this window size the algorithm would be able to effectively locate the core of the PV. The convergence analysis was also important because as the window increases, the the longer the Gamma algorithm takes to execute. This is a computationally intensive and expensive process, so cost savings are important. The flow field size input into the analysis was also restricted to decrease the time required to run the calculation. This could be done, because the general location of the passage vortex was already known from the time average of Q. This also meant that the noisy regions on the edge of the data sets would not interfere with the calculation.

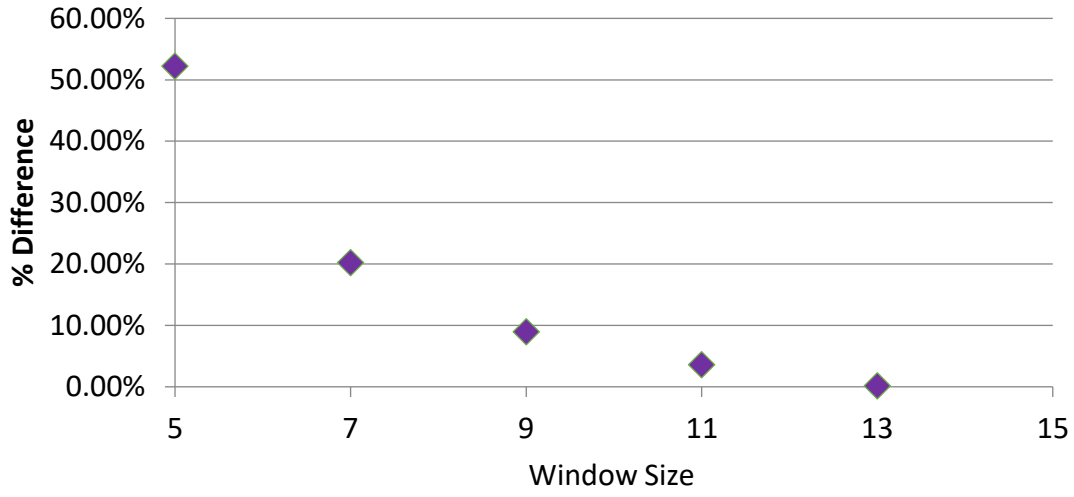

Figure 44: Convergence analysis for the window size for the Gamma method.

The results for the location of the core found using the Gamma criteria are shown in Figure 45. The value of Γ_1 at the core of a vortex should ideally have a value close to 0.9 or 1. For these data sets, however, the maximum was typically around 0.3. This was due to the fact the PV is not an ideal vortex shape. The PV is not perfectly round nor is it perfectly normal the SPIV plane. These results show that at a $F^+ = 1.2$, the PV was located the closest to the suction surface which is consistent to the results from using Q. This plot, however, has a slightly different shape at a frequency of $F^+ = 0.8$. The core of the PV was closer to the pressure surface. This did not occur in the results using Q. The PV was the closest to the suction surface when pulsing at $F^+ = 1.2$ and was located at roughly 0.215 axial chord. This contrasted with the results found using Q for the analysis. Based on Q, it was located at 0.2 axial cord, which is a percent difference of 7.5%.

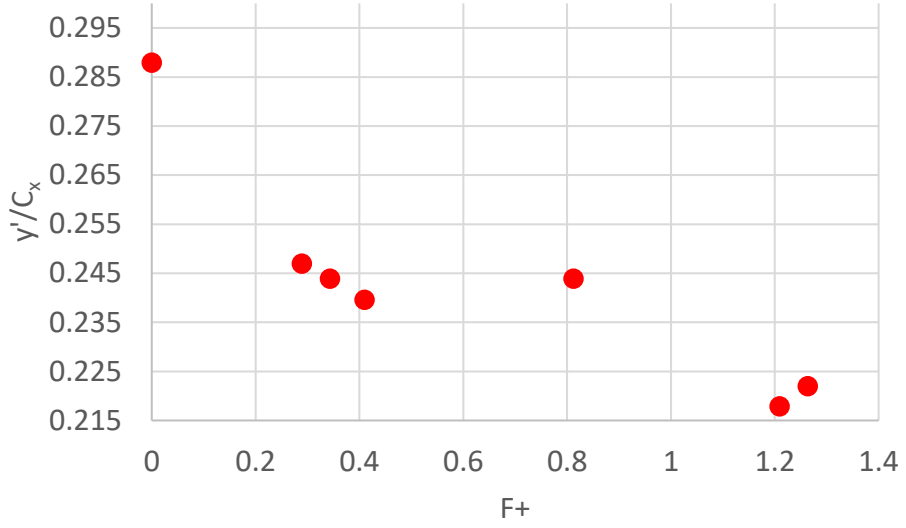

Figure 45: Pitchwise location of PV core calculated using the Gamma method.

4.6 Hot-film sensor results for baseline and 22 and 65 Hz results

The results for a single hot-film sensor that was placed slightly downstream of the SPIV plane and aligned with the PV are shown in Figure 46. The results presented are for the baseline flow condition and endwall pulsing for the frequencies $F^+ = 0.4$ and $F^+ = 1.2$. For the baseline flow condition, spectral analysis of the hot-film sensor data showed frequency bands present at low frequencies. Since the hot-film was placed across the PV lift-off line these frequencies corresponded to the PV oscillation frequencies. There are small frequencies centered around $F^+ = 0.4$ which matched what Veley et al. had previously found using hot-film sensors to study the flow [15]. These are also similar frequencies that were present in the PSD of Q, Figure 19.

For the F+ = 0.4 frequency, the same sensor showed the peaks that were present at the lower frequencies in the baseline condition are now gone. Instead, there were now peaks present in the PSD of the sensor with relatively large magnitudes at $F^+ = 0.4$ and 0.8. The

peak that was present at $F^+ = 0.8$ has a magnitude of less than a third of the peak present at $F^+ = 0.4$. This peak was most likely present at F+ = 0.8 since it is a harmonic of the jet pulsing frequency. These peaks were due to the oscillations of the PV or the jet artifact since the hot-films were located across the PV lift-off line and downstream of the jets.

For the $F^+ = 1.2$ case, there are peaks in the PSD of the hot-films at $F^+ = 1.2$. Also, the peaks at the lower frequencies are gone like they were for the $F^+ = 0.4$ pulsing frequency. The peak was much lower than it was for the $F^+ = 0.4$ case, however, this could be because the PV had moved closer to the suction surface and this sensor was close to the pressure surface. The peaks at the pulsing frequencies along with the removal of low frequency responses present in the baseline results reinforced the hypothesis that the PV movement locked in with the pulsing frequencies.

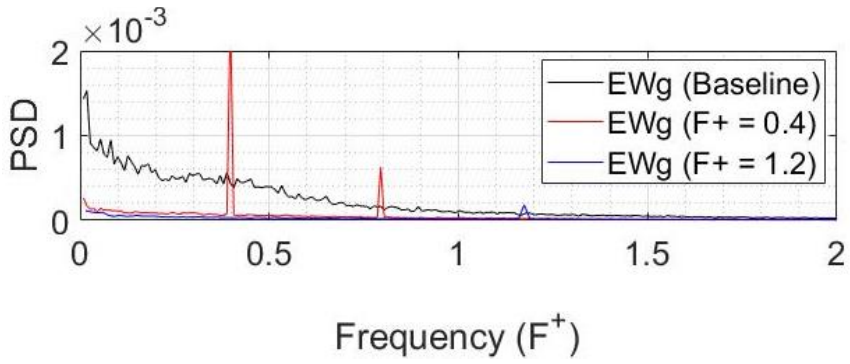

Figure 46: PSD from a single hot-film sensor for the baseline, F+ = 0.4 pulsing, and F= = 0.8 pulsing at Re = 100k

4.7 PSD of Q for the F+ = 0.4 and F+ = 1.2 pulsing cases

The PSD of Q was calculated for the cases of $F^+ = 0.4$ and 1.2. This was done to confirm the results from the hot-film sensor. The frequencies at which peaks for the pulsed cases were seen in the hot-films were investigated across the flow field. In Figure 47, the magnitude of the PSD of the F+ = 0.4 frequency for the F+ = 0.4 pulsing case is shown.

This demonstrates that there were peaks present at this frequency at the locations between which the PV moves. Implying, that this was the frequency at which the PV oscillates. This also confirms that the PV oscillations locked in with the pulsing frequency at this frequency.

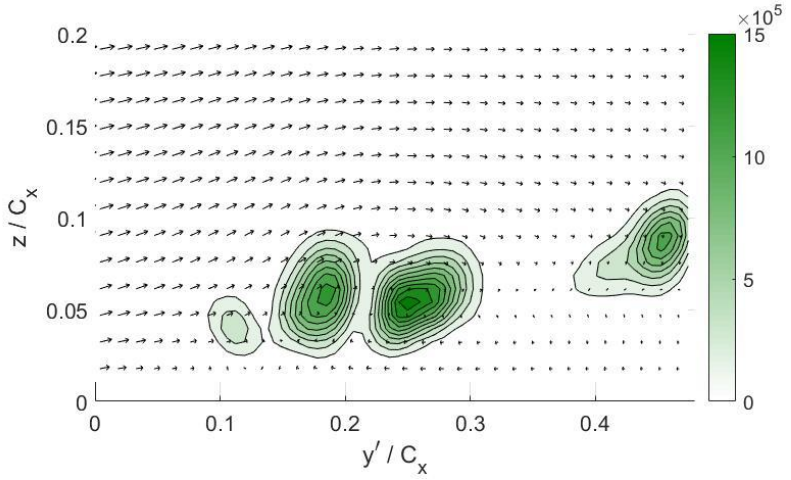

Figure 47: Magnitude of the PSD for the $F^+ = 0.4$ for the endwall pulsing frequency of $F^+ = 0.4$.

The harmonic of the F+ = 0.4 PSD of Q was also investigated since there were peaks present in the hot-film sensors for the F+ = 0.4 endwall jet pulsing case, Figure 48. These peaks were present in approximately the same location as the F+ = 0.4 peaks. These are most likely present because they are a harmonic frequency of F+ = 0.4. Certain smaller oscillations could also have occurred at this frequency.

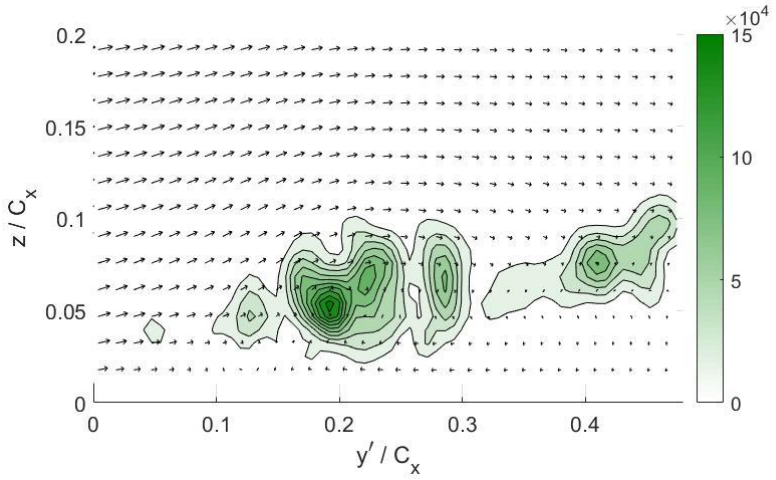

Figure 48: Magnitude of the PSD of Q for the F^+ = 0.8 for the endwall pulsing frequency of F^+ = 0.4.

Figure 49 is the magnitude of the PSD of Q at the F+ = 1.2 frequency for the endwall jet pulsing case of F+ = 1.2. There were peaks in the hot-film sensors present at this frequency. Figure 49 confirms that the PV oscillated at this frequency. This confirms that the PV oscillations and behavior does in fact lock in with the pulsing frequency of the endwall jets.

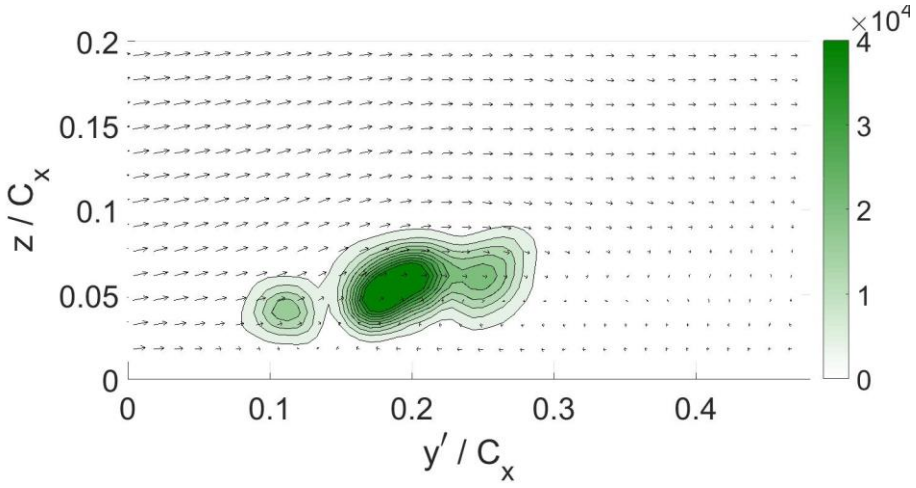

Figure 49: Magnitude of the PSD for the F^+ = 1.2 for the endwall pulsing frequency of F^+ = 1.2.

4.8 Baseline flow Re = 50k vs baseline Re = 100k

The final objective of this research was to characterize the baseline flow at a Reynolds number of 50k. The time average Q for the baseline flow at a Reynolds number of 50k is shown in Figure 50. The PV has a width of $0.15C_x$ in the pitchwise direction. This is larger than the $0.1C_x$ width for the baseline flow at 100k Reynolds number. The PV also has a larger spread in the spanwise direction of $0.075C_x$ vs $0.05C_x$ for the flow at a Reynolds number of 100k. Therefore, the PV moved more in the spanwise direction at a Reynolds number of 50k. The time average of Q shows that the PV was weaker at the Reynolds number of 50k vs 100k. At 50k, the PV had a maximum strength of 150 in the area surrounding the core while at 100k the strength was 200. The second vortex that was present under the secondary shear layer at the Reynolds number of 100k was still present in the 50k results. The second vortex was still located near the $0.14C_x$, however, it was weaker than at 100k.

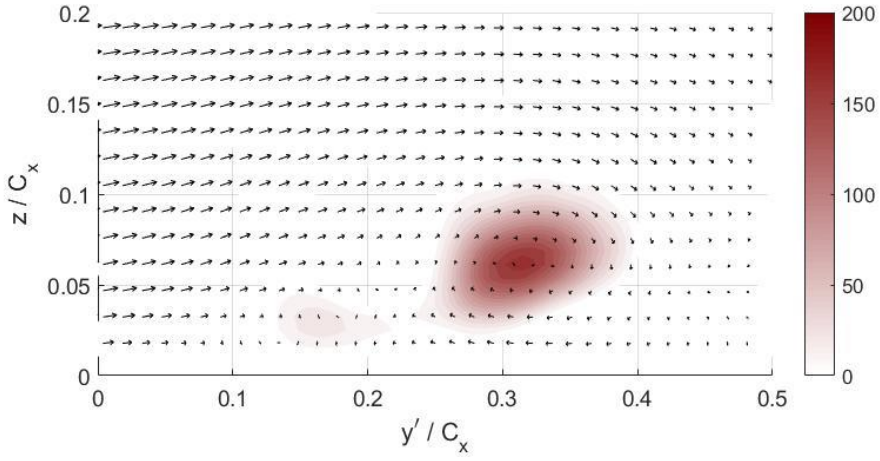

Figure 50: Time average Q for baseline for at Re = 50k.

Figure 51 shows the plot of the Q for both 50k and 100k. Clearly, for a Reynolds number of 50k the PV is located closer to the pressure side. In both cases there was a second vortex

present beneath the secondary shear. For 50k, the second vortex mean position was located closer to the pressure side.

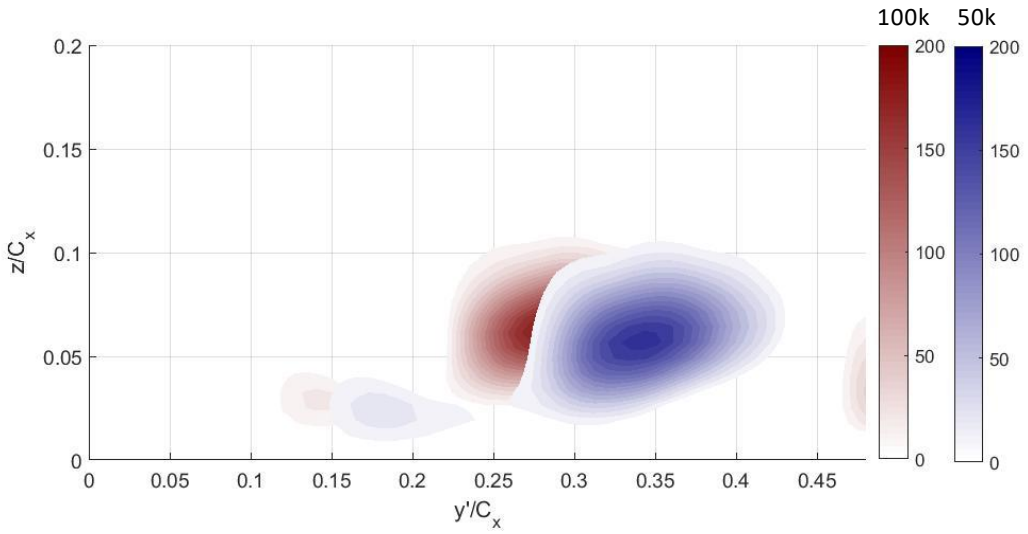

Figure 51: Mean Q values for baseline flow at Re = 100k and Re = 50k.

Figure 52 shows the value of Q for four different instantaneous points in time. These points in time are different than were picked for the Reynolds number of 100k. They were randomly selected. These demonstrate that, the PV intermittently lost coherence and its position changed. It is also clear from these snapshots that the PV was still the dominate flow structure, however, there were smaller weaker vortices. The smaller vortices must not have been present for most of the time since they do not appear in the time average results. The PV pitchwise position still moved significantly with time. These plots also confirmed the PV moved more in the spanwise direction, at a Reynolds number of 50k than it did at 100k.

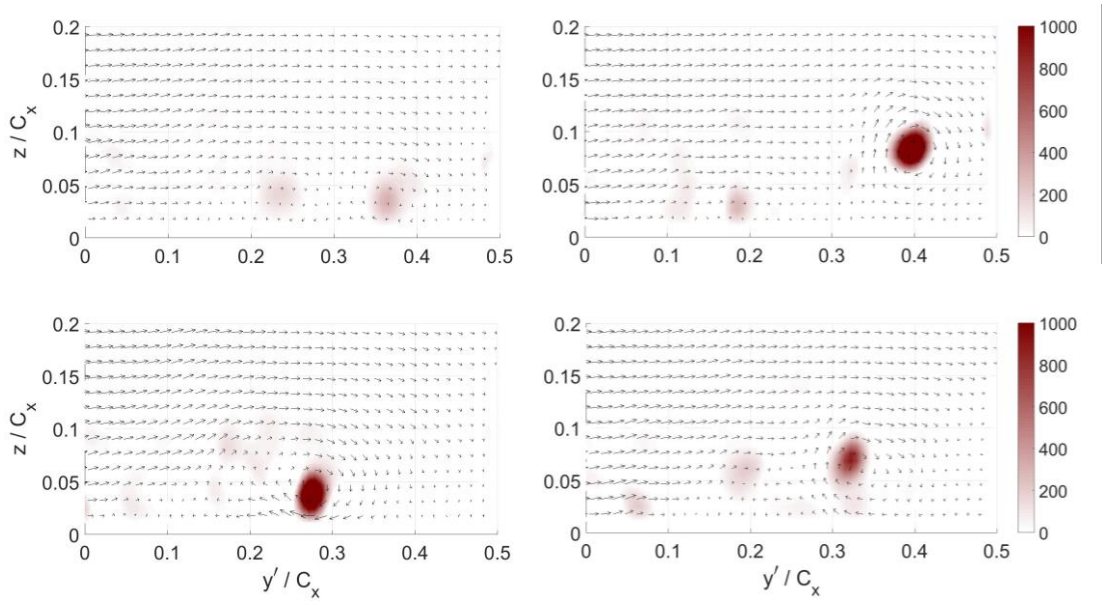

Figure 52: Instantaneous plots of Q for baseline flow at Re = 50k.

The instantaneous values of the ratios of the peak Q to the average peak Q and the pitchwise position of the PV with respect to time are shown in Figure 53. Clearly, the PV position and strength moved greatly with respect to time. There were also events that corresponded to a rapid increase and loss of strength. These also corresponded to a rapid change in the position of the PV, similar to the 100k Reynolds number results. These events are labeled A – C in Figure 53, and occurred on time scales between $3.8 < \Delta T^{+} < 4.6$. These are different from the time scales for the 100k results. For 100k, the events occurred at times scales between $1.9 < \Delta T^{+} < 6.7$. This means that there was less variability in the time between the events at 50k.

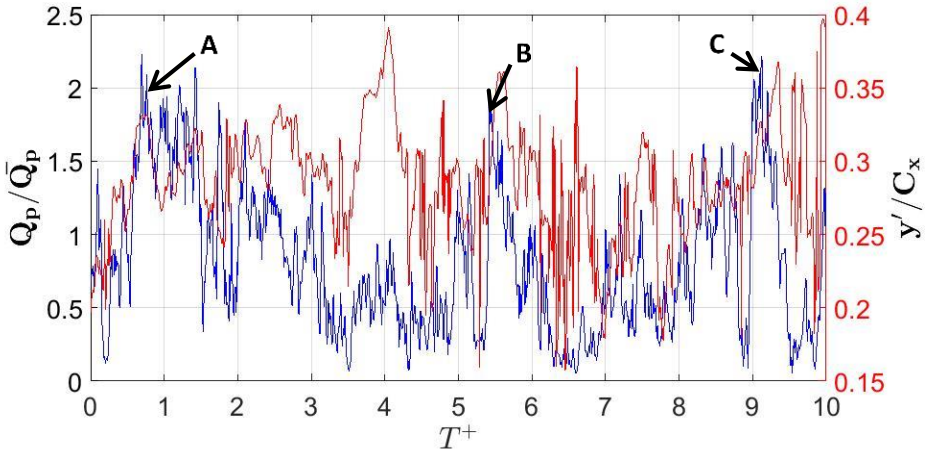

Figure 53: Instantaneous value of peak Q and pitchwise position.

In Figure 54, the instantaneous values of the peak Q ratio and the pitchwise position are shown. The values for the first five convective times are shown, making the intermittent fluctuations clearer. The PV does not experience smaller events between the larger events as occurred for 100k. For the 100k results, the PV lost strength and fluctuated about a low strength for a significant period of time. This did not occur for the 50k results.

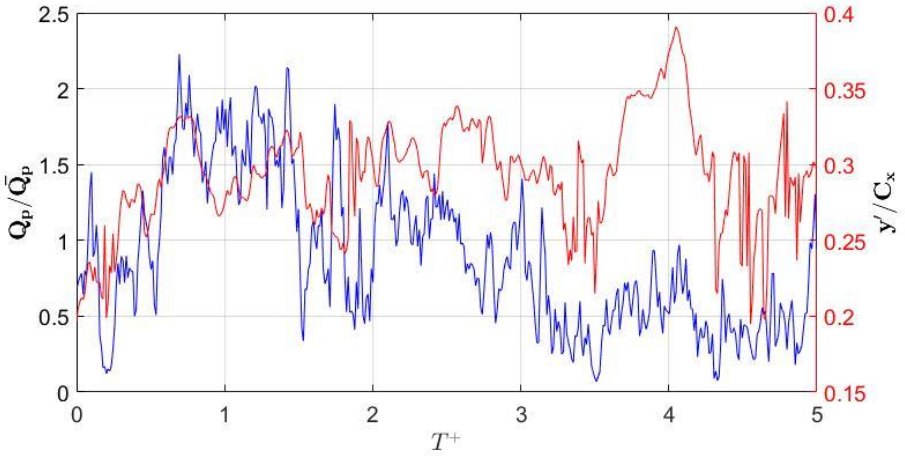

Figure 54: Instantaneous value of peak Q and pitchwise position for 5 convective times.

Figure 55 shows the PSD of the magnitude of Q for the signal at a frequency of F+ = 0.4 frequency for the 50k data. This was the frequency with the largest peak for the 100k case. The signal is an order of magnitude weaker for the 50k results than the 100k. The shape of the signal is also different. Instead of having two clear peaks in roughly the same spanwise locations but different pitchwise locations, there is a larger spanwise spread with more than two large peaks. These means that the PV still oscillated at this frequency. However, it moved more significantly in the spanwise direction than the 100k results.

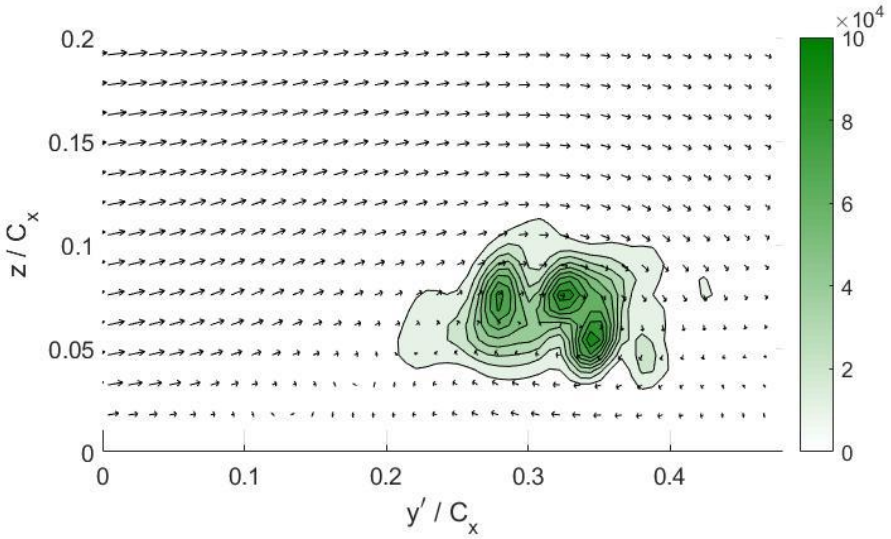

Figure 55: Magnitude of the PSD for the F^+ = 0.4 for the baseline flow

The circulation of the PV at 100k was also calculated over a 2s time interval. This was done to determine how the strength changes over a relatively large period, since it was found that circulation is a better representation of the overall strength of the PV. It accounts for the entire vortex rather than just a core. The circulation of the PV for 50k is given in Figure 56. When comparing these results to the 100k results, Figure 23, the results for 50k are more consistent over the same time period. The strongest values of circulation are all

closer together over the ten convective times, and the PV loses and gains strength more consistently.

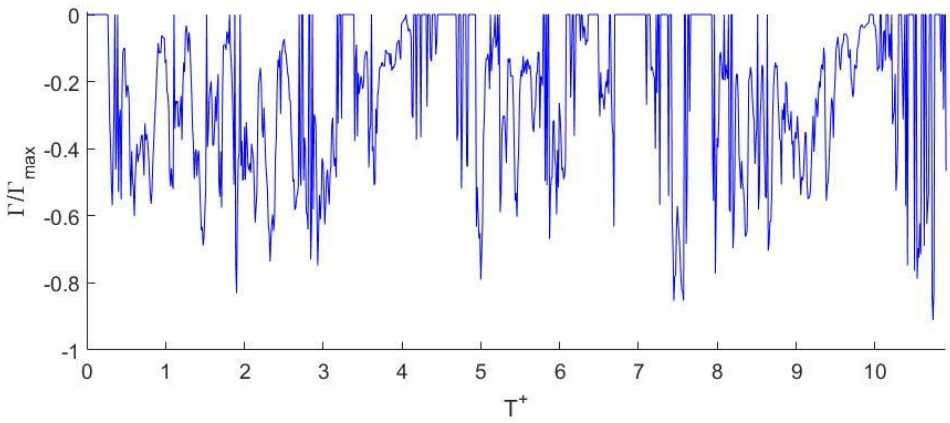

Figure 56: Circulation for the baseline flow at Re = 50k over ten convective times.

Figure 57 shows the same data presented in Figure 56, however, it is zoomed in on the first five convective times. According to the circulation, it appears that the PV fluctuated around a strength roughly 25% of the maximum strength in between the large events of change in coherence. This was true for the PV at 100k, however, this was not true for the plot of the peak Q ratio at 50k which had been shown in Figure 54. Circulation is representative of the strength of the entire vortex, which Q did not. This could account for the differences between Q and circulation.

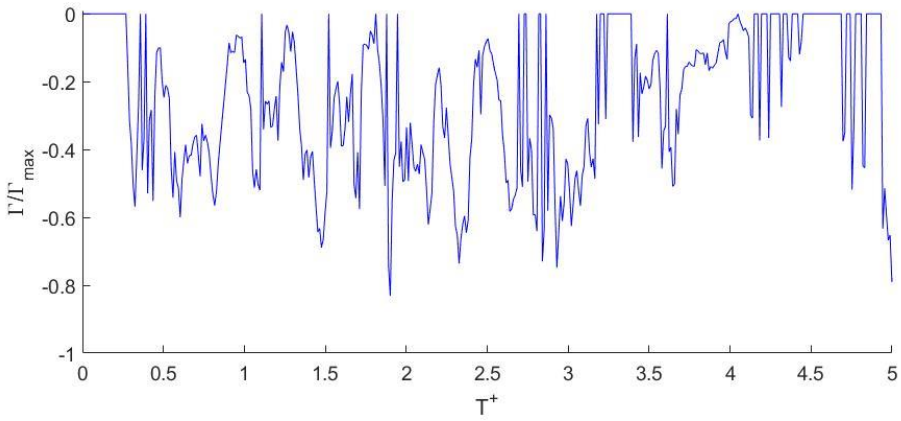

Figure 57: Circulation for the baseline flow at a Re = 50k for five convective times.

The time average of the turbulent kinetic energy at 50k is shown in Figure 58. By comparison to the results for the TKE for 100k, presented in Figure 20, the amount of fluctuations are similar in both causes. In both cases the largest TKE occurred near the PV. This was expected since previous research showed that the PV moves with time.

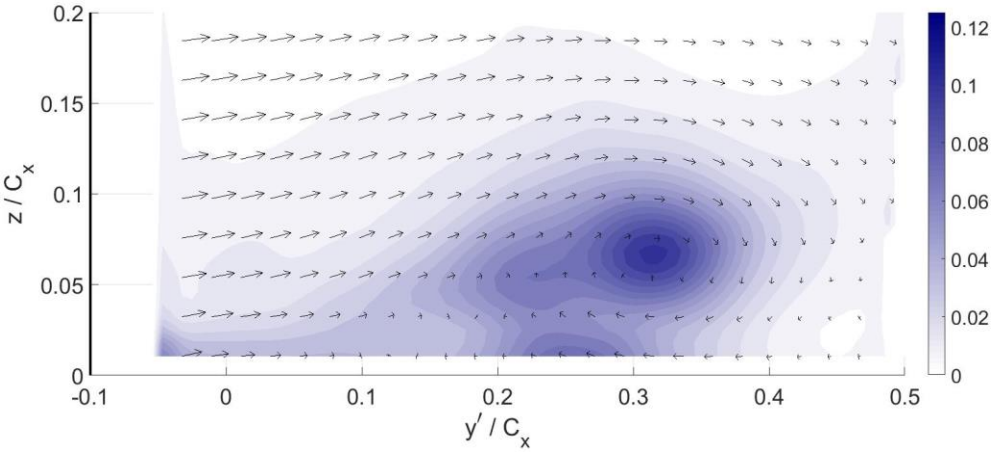

Figure 58: Time average of the TKE for the baseline flow at a Reynolds number of 50k.

5. Conclusions

One of the main objectives of this research was to characterize the PV for the baseline flow at a Reynolds number of 100k. The baseline PV dramatically changes in both strength and position with time. The PV peak strength as quantified by Q varied over 80% and the position changes over 20% axial chord (16% pitch spacing) with time in a quasi-periodic manner (broad spectrum centered around 22Hz, F^+ 0.4). In the time resolved data sets acquired, there were large events that occur between $1.9 < \Delta T^+ < 6.7$ which corresponded to dramatic and rapid changes in core strength and position. There were also smaller events that occurred between the larger events and these occurred at times between $0.7 < \Delta T^+ < 1.5$. It was found that between the large events the PV oscillated for extended times at 25% of the maximum core strengths.

Another objective of the study was to determine how the pulsed endwall jets affected the flow through the passage, especially the effect on the PV. It is clear the pulsed jets had a significant effect on the flow field. At all pulsing frequencies, the jets weakened the PV and shifted it closer to the suction surface. It is also clear that the frequency at which the jets were pulsed effected the PV in different ways. At a pulsing frequency of F+ = 0.4, the jets caused the PV to split or for a second vortex to form. Currently, it is not possible to determine which it was. Additional planes of SPIV data would be needed to determine this. The second vortex appeared 40% of the way through the pulsing period. This was the same

time the jets are observed to be passing through the SPIV plane. Therefore, this could be the cause – again more SPIV data would be required to know for certain the cause.

The endwall jets increased the TKE when their effects passed through the SPIV plane. The time averaged TKE for the pulsed cases was much lower, making it clear that the endwall jet pulsing stabilized the PV. This implies that the endwall jets caused the PV to lock in with the pulsing frequency, which was the opposite of what Gross et al. believed would lead to a reduction [27]. This was confirmed by the results for the surface mounted hot-film sensors. The hot-film sensors had peaks in the PSD at the pulsing frequencies for the pulsed endwall jet cases, meaning that the PV oscillated at these frequencies. There were peaks at lower frequencies for the baseline flow condition that corresponded to the frequencies at which the PV lost its coherence and oscillated between its locations. These frequency bands were no longer present for the pulsed cases. This was also confirmed by plotting the PSD of Q across the PSIV plane.

It was found for the endwall jet pulsing frequency of F+ = 1.2 that the PV core was located closest to the suction surface when analyzed by both Q and the Gamma method. This was also the frequency at which the PV was the weakest according to both Q and the calculated circulation. F+ = 1.2 was the frequency that had previously been found to correspond to the maximum total pressure loss reduction and improvement in the exit angle. This implies that weakening the PV in combination with shifting it toward the suction surface led to the largest reductions in loss and exit angle improvements. This was different than previous findings which determined moving the PV away from the suction surface led to a loss reduction, since that prevented it from reacting with the boundary layer in that region.

Another objective was to fully characterize the baseline flow at a Reynolds number of 50k. It was found that at this flow condition the PV still intermittently lost its strength and coherence as well as changed in position. There were still large events that occurred which corresponded to drastic changes in strength and position. These occurred at times $3.8 < \Delta T^{+} < 4.6$, which were different than the times for the baseline Reynolds number of 100k flow condition. The PV still was the dominate vortex in the flow field and moved significantly in the pitchwise direction between the suction and pressure surface. It was found that at 50k the PV moved more significantly in both the pitchwise and spanwise directions than the 100k flow.

Several different methods of processing were used to determine both the location and strength of the PV. Q was the best way to locate the position of the PV. This is because the PV was not an ideal vortex and was not always normal to the SPIV plane. The circulation was the best measure of the strength of the core of the vortex because it accounts for the entire vortex strength rather than at a single point.

6. Future Work

To determine how the effects of the jets propagate through the passage, it would be beneficial to investigate how the PV changes position and strength through the passage. It would also be beneficial to better characterize the flow coming out of the jets. This would give insight into the vortical structures that are directly created by the endwall jets. It would also help determine how far the jets are penetrating the flow at each of the pulsing conditions, and whether the jets are essentially emulating a well understood flow control method such as an endwall fence or are in fact operating through a fluid-dynamic interaction. Implementing the pulsed jets with a wake generator could also provide a more accurate representation as to how effective they would be in an LPT. It would test how the endwall jets would interact with wakes like those that would be present in an LPT. Investigating both the baseline flow field and the flow with the pulsed jets using Tomographic Particle Image Velocimetry (TPIV) would also be beneficial. TPIV would provide a three-dimensional visualization of the PV which would aid it determining the mechanisms driving the losses.

References

[1] R. J. Howell, H. P. Hodson, V. Schulte, R. D. Stieger, H.-P. Schiffer, F. Haselbach and N. W. Harvey, "Boundary Layer Development in the BR710 and BR715 LP Turbines—The Implementation of High-Lift and Ultra-High-Lift Concepts," *Journal of Turbomachinery,* vol. 124, no. July, pp. 385-392, 2002.

[2] K. A. Gompertz and J. P. Bons, "Combined Unsteady Wakes and Active Flow Control on a Low-Pressure Turbine Airfoil," *Journal of Propulsion and Power,* pp. 990-1000, 2011.

[3] O. P. Sharma and T. L. Butler, "Predictions of Endwall Losses and Secondary Flows in Axial Flow Turbine Cascade," *Journal of Turbomachinery,* vol. 109, no. 4, pp. 229-236, 1987.

[4] L. S. Langston, "Secondary Flows in Axial Turbines - A Review," *Heat Transfer in Gas Turbine Systems,* vol. 934, no. 1, pp. 11-26, 2001.

[5] N. V. Aunapu, R. J. Volino, K. A. Flack and R. M. Stoddard, "Secondary Flow Measurements in a Turbine Passage with Endwall Flow Modification," in *ASME Turbo Expo*, Munich, 2000.

[6] L. S. Langston, M. L. Nice and R. M. Hooper, "Three-Dimensional Flow Within a Turbine Cascade Passage," *Journal of Engineering for Power,* vol. 99, no. 1, pp. 21-28, 1977.

[7] J. Bons, S. Benton, C. Bernardini and M. Bloxham, "Active Flow Control for Low-Pressure Turbines," *AIAA Journal*, pp. 2687-2698, 2018.

[8] C. H. Sieverding, "Recent Progress in the Understanding of Basic Aspects of Secondary Flows in Turbine Blade," *Journal of Engineering for Gas Turbines and Power,* vol. 107, pp. 247-257, 1985.

[9] R. J. Volino, "Separation Control on Low-Pressure Trubine Airfoils Using Synthetic Vortex Generator Jets," *Journal of Turbomachinery,* vol. 125, no. 10, pp. 765-777, 2003.

[10] A. Gross, C. R. Marks and R. Sondergaard, "Numerical Investigation of Low-Pressure Turbine Junction Flow," *AIAA Journal,* pp. 1-5, 2017.

[11] P. Bear, M. Wolff, A. Gross, C. R. Marks and R. Sondergaard, "Experimental Investigation of Total Pressure Loss Development in a Highly Loaded Low-Pressure Turbine Cascade," *Journal of Turbomachinery*, pp. 1-9, 2018.

[12] C. R. Marks, R. Sondergaard, P. Bear and M. Wolff, "Reynolds Number Effects on the Secondary Flow of Profile Contoured Low Pressure Turbines," in *AIAA SciTech Forum*, San Diego, 2016.

[13] P. Bear, M. Wolff, A. Gross, C. R. Marks and R. Sondergaard, "Secondary Loss Production Mechanisms in a Low Pressure Turbine Cascade," in *AIAA Propulsion and Energy Forum*, Salt Lake City, 2016.

[14] A. Gross and R. Sondergaard, "Investigation of Low-Pressure Turbine Endwall Flows: Simulations and Experiments," in *AIAA Scitech Forum*, Kissimmee, 2015.

[15] E. Veley, C. R. Marks, R. Anthony, R. Sondergaard and M. Wolff, "Unsteady Flow measurements in a Front Loaded Low Pressure Turbine Passage," in *AIAA SciTech Forum*, Kissimmee, 2018.

[16] E. Veley, C. R. Marks, R. Anthony, R. Sondergaard, N. Fletcher and M. Wolff, "Unsteady Flow Measurements in a Low Pressure Turbine Passage using Surface mounted Thin-Film Sensors," in *AIAA Propulsion and Engery Forum*, Atlanta, 2017.

[17] M. J. Bloxham and J. J. Bons, "A Global Approach to Turbomachinery Flow Control: Passage Vortex Control," *Journal of Turbomachinery*, pp. 1-9, 2014.

[18] C. Bernardini, S. I. Benton and J. P. Bons, "The Effect of Acoustic Excitation on Boundary Layer Separation of a Highly Loaded LPT," *Journal of Turbomachinery*, vol. 135, no. 8, pp. 1-9, 2013.

[19] J. Dickel, C. R. Marks, R. Sondergaard and M. Wolff, "Optimization of a Non-Axisymmetric Endwall Contour for Front-Loaded High-Lift Low Pressure Turbines Jacob," in *AIAA Propulsion and Energy Forum*, Cincinnati, 2018.

[20] J. Dickel, C. R. Marks, J. Clark, R. Sondergaard and M. Wolff, "Non-Axisymmetric Endwall Contouring of Front-Loaded High-Lift Low Pressure Turbines," in *AIAA SciTech Forum*, Kissimmee, 2018.

[21] N. Fletcher, C. R. Marks, R. Petrie, R. Sondergaard and M. Wolff, "Experimental Investigation of Endwall Flow Control for Front-Loaded Turbine Blades," in *AIAA Propulsion and Energy Forum*, Cincinnati, 2018.

[22] E. M. Veley, "Measurement of Unsteady Characteristics of Endwall Vortices Using Surface-Mounted Hot-Film Sensors," Wright State University, Dayton, 2018.

[23] J. C. R. Hunt, A. A. Wray and P. Moin, "Eddies, Streams, and Convergence Zones in Turbulent Flows," in *Center for Turbulence Research*, Stanford, 1988.

[24] M. E. Boghosian and K. W. Cassel, "On the origins of vortex shedding in two-dimensional incompressible flows.," *Theoretical and Computational Fluid Dynamics*, vol. 30, no. 6, pp. 511-527, 2016.

[25] A. Gross and Z. Robison, "Numerical Simulations of Turbulent Junction Flow," in *Fluid Dynamics Conference*, Atlanta, 2018.

[26] L. Graftieaux, M. Michard and N. Grosjean, "Combining PIV, POD, and vortex identiification algorithms for the study of unsteady trubulent swirling flows," *Measurement Science and Technology*, vol. 12, no. 9, pp. 1422-1429, 2001.

[27] A. Gross, C. Marks and R. Sondergaard, "Numerical Simulations of Active Flow Control for Highly Loaded Low-Pressure Turbine Cascade," in *AIAA Scitech Forum*, Grapevine, 2017.